Ice nucleation abilities of soot particles determined with the Horizontal Ice Nucleation Chamber

Fabian Mahrt[1], Claudia Marcolli[1], Robert O. David[1], Philippe Grönquist[3,4], Eszter J. Barthazy Meier[2], Ulrike Lohmann[1], and Zamin A. Kanji[1]

[1]Department of Environmental System Sciences, Institute for Atmospheric and Climate Science, ETH Zurich, 8092 Zurich, Switzerland
[2]Scientific Center for Optical and Electron Microscopy, ETH Zurich, 8093 Zurich, Switzerland
[3]Department of Civil, Environmental and Geomatic Engineering, Institute for Building Materials, ETH Zurich, 8093 Zurich, Switzerland
[4]Department of Functional Materials, Applied Wood Materials, Empa, 8600 Dubendorf, Switzerland

Correspondence: F. Mahrt (fabian.mahrt@env.ethz.ch) and Z. A. Kanji (zamin.kanji@env.ethz.ch)

Abstract. Ice nucleation by different types of soot particles is systematically investigated over the temperature range from 218 to 253 K relevant for both mixed-phase (MPCs) and cirrus clouds. Soot types were selected to represent a range of physicochemical properties associated with combustion particles. Their ice nucleation ability was determined as a function of particle size using relative humidity (RH) scans in the Horizontal Ice Nucleation Chamber (HINC). We complement our ice

5   nucleation results by a suite of particle characterization measurements, including determination of particle surface area, fractal dimension, temperature dependent mass loss, water vapor sorption and inferred porosity measurements. Independent of particle size, all soot types reveal absence of ice nucleation below and at water saturation in the MPC regime ($T > 235$ K). In the cirrus regime ($T \leq 235$ K), soot types show different freezing behaviour depending on particle size and soot type, but the freezing is closely linked to the soot particle properties. Specifically, our results suggest that if soot aggregates contain mesopores (pore

10   diameters of $2-50\,\mathrm{nm}$) and have sufficiently low water-soot contact angles, they show ice nucleation activity and can contribute to ice formation in the cirrus regime at RH well below homogeneous freezing of solution droplets. We attribute the observed ice nucleation to a pore condensation and freezing (PCF) mechanism. Nevertheless, soot particles without cavities of the right size and/or too high contact angles nucleate ice only at or well above the RH required for homogeneous freezing conditions of solution droplets. Thus, our results imply that soot particles able to nucleate ice via PCF, could impact the microphysical

15   properties of ice clouds.

1 Introduction

Soot, mainly composed of highly agglomerated carbon spherules, is a by-product of incomplete combustion of biomass and fossil fuels and represents a major anthropogenic pollutant. Globally, emissions of soot are estimated to reach 7500 Ggy^{-1}

(uncertainty range: $2000 - 29000$ Ggy^{-1}, Bond et al., 2013), with a direct source in the upper troposphere from aviation emissions, and thus are of high relevance for climate (Ramanathan and Carmichael, 2008). Soot aerosols generally denote complex internal mixtures of black carbon (BC) and associated organic matter (OM, Petzold et al., 2013), and here we use the term *soot* to encompass internal mixtures of both. Soot aggregates usually have diameters on the nanoscale, ranging from

5   individual primary carbonaceous spherules to large, fractal-like aggregates (Adachi et al., 2007). The primary particle diameter itself can vary from around 10 nm to several hundred nanometers, depending on the combustion source. The diverse physicochemical properties of soot aerosols make an analytical assessment of their environmental effects challenging. Soot particles can act as ice nucleating particles (INPs, Vali et al., 2015) in cirrus clouds (DeMott, 1990; DeMott et al., 1999) and MPCs as well as in aircraft contrail formation (Seinfeld, 1998; Boucher, 1999; Popovicheva et al., 2004; Schumann, 2005; Kärcher

10   et al., 2007; Heymsfield et al., 2010; Schumann and Heymsfield, 2017; Kärcher, 2018) and thus affect cloud properties such as emissivity, lifetime, albedo and cloud coverage. The pathways of ice formation have recently been reviewed by Vali et al. (2015) and Kanji et al. (2017). For instance, when acting as INPs in supercooled liquid and/or MPCs, aerosol particles can trigger glaciation of the clouds resulting in efficient precipitation formation causing a reduction in cloud lifetime (Lohmann, 2002). However, this so-called glaciation effect is rather uncertain due to unknowns in primary ice formation with aerosol

15   species such as soot (Lohmann, 2002). Additionally, particle properties such as coatings of BC with organic substances can reduce or inhibit their ice nucleation abilities (Hoose et al., 2008) thus adding further uncertainties to the contribution of soot to ice nucleation. Understanding the ice nucleation mechanism of soot aerosols is crucial in order to describe the fate of these particles in the atmosphere and resolve the uncertainties associated with aerosol-cloud interactions (Lohmann, 2015; Fan et al., 2016; Lohmann and Feichter, 2005). This will ultimately enhance our understanding of the anthropogenic influence on clouds.

   Numerous laboratory studies have investigated the ice nucleation ability of soot (e.g. DeMott, 1990; Diehl and Mitra, 1998; DeMott et al., 1999; Gorbunov et al., 2001; Suzanne et al., 2003; Popovicheva et al., 2004; Möhler et al., 2005a, b; Dymarska et al., 2006; Kanji and Abbatt, 2006; DeMott et al., 2009; Fornea et al., 2009; Koehler et al., 2009; Kanji et al., 2011; Crawford et al., 2011; Chou et al., 2013; Brooks et al., 2014; Kulkarni et al., 2016; Schill et al., 2016; Charnawskas et al., 2017; Demird-

25   jian et al., 2009; Kireeva et al., 2009). However, these studies have revealed a large variability in ice nucleation characteristics of soot particles, indicating that the ice formation ability of soot remains poorly understood. For instance, DeMott et al. (1999) used commercially available lamp black soot (Degussa) to test the ice nucleation ability of soot in the cirrus regime ($T \leq 235$ K), using a continuous flow diffusion chamber (CFDC). They found ice formation below water saturation for $T < 231$ K. However, since ice nucleation was observed very close to water saturation, whether the ice formation occurred through deposi-

30   tion nucleation or water sorption and subsequent freezing could not be determined. This finding is in direct contrast to Möhler et al. (2005a), who used soot produced by a graphite spark generator (GSG) and tested its ice nucleation ability using the AIDA (Aerosol Interactions and Dynamics in the Atmosphere) chamber. They found bare (uncoated) GSG soot to nucleate ice in the deposition mode for $T < 233$ K, with ice formation onset observed well below homogeneous freezing conditions, even though their reported activated fractions made up only 0.3 % of the total aerosol population. Investigation of ice nucleation

35   on propane fuel particles by Möhler et al. (2005b) revealed a dependence of the ice nucleation ability on the OM content of

the soot particles. They showed that ice nucleation at 207 K on low OM soot (16 % by mass) was more efficient compared to high OM content (40 % by mass) particles. While the ice nucleation onset for the low OM soot was similar to that observed by Möhler et al. (2005a) for H_2SO_4 coated GSG soot, the high OM soot required homogeneous freezing conditions. The cause for this was interpreted as a suppression of deposition nucleation by the increased organic content covering the carbon spherules.

5 A later study by Crawford et al. (2011) on the ice nucleation of propane soot particles came to the same conclusion by varying OM content. Specifically, they found that only the soot particles with the lowest OM content (5 % by mass) were able to heterogeneously nucleate ice in the deposition mode (at $T = 226$ K), while higher OM content soot (30 % and 70 % by mass) required water supersaturation. Friedman et al. (2011) performed ice nucleation experiments on size selected soot particles produced by a propane burner at $T = 233$ K, 243 K and 253 K. They did not detect heterogeneous ice formation of bare soot

10 particles before the formation of cloud droplets. At the same time they found that organic coatings resulted in an increased hydrophilicity, but not in a significant change in the ice nucleation ability of the particles. Koehler et al. (2009) tested the ice nucleation ability of five different soot types with different physicochemical properties in the cirrus regime. They reported that the capacity of the soot particles to take up water strongly influenced their ice nucleation characteristics. Using the hydration property classification described in Popovicheva et al. (2008), they found hygroscopic soot, with water uptake caused by water-

15 soluble material on the soot aggregates, to freeze only homogeneously, similar to any other hygroscopic particles. In contrast, hydrophobic and hydrophilic soots, associated with little or no water-soluble material both froze heterogeneously. The authors therefore concluded that water affinity alone is insufficient to predict the ice nucleation ability of soot and that other particle characteristics such as porosity and surface polarity complicate predictions for the heterogeneous freezing of soot particles. A direct intercomparison of the ice nucleation results discussed above is challenging due to the complex characteristics of soot

20 particles. Yet, the heterogeneity of the reported ice nucleation results arise partly from the irreproducibility associated with combustion particle properties (Popovicheva et al., 2008) and from the different techniques used to probe ice nucleation.

In this study we systematically investigate the ice formation ability of six different soot samples. Testing the ice nucleation of soot particles with different physicochemical properties using the same experimental procedure, allows for a direct comparison and improves our understanding of the ice formation characteristics of soot aerosol. Ice nucleation was investigated in the

25 MPC ($T > 235$ K) and cirrus cloud temperature regime, covering the range between $218 - 253$ K, as a function of relative humidity (RH) and aerosol size, using the Horizontal Ice Nucleation Chamber (HINC, Lacher et al., 2017), a continuous flow diffusion chamber. Our measurements extend the limited measurements of particle size dependent ice nucleation characteristics of soot aerosol, particularly in the cirrus regime. In addition, we characterize the particle properties and report measurements of morphological features, bulk heat sensitive fraction, hydrophilicity and porosity of the soot samples to interpret our INP

30 measurements. By combining these auxiliary measurements with our INP experiments, we draw fundamental conclusions on the relationship between particle properties and the ice formation mechanisms of soot particles for atmospherically relevant conditions.

2 Experimental methods and materials

2.1 Soot samples

Soot samples were chosen to represent a wide range of combustion aerosol physicochemical properties as proxies of atmospheric soot and to allow for a direct comparison to previous studies. A summary of the characteristics of the soot samples used here is shown in Table 1. Below we briefly describe their properties and origin.

FW200: This commercially available carbon black (Orion Engineered Carbons GmbH, OEC, Frankfurt, Main, Germany) is produced in the gas black process, through the incomplete combustion of liquid hydrocarbons. A commercial carbon black was chosen to ensure reproducibility of the sample for future ice nucleation studies. The gas black method allows for production of particles with narrow primary particle size distributions with mean primary particle diameters of $\bar{d}_{pp} = 22$ nm, as found by transmission electron microscopy (TEM, see Table 1). The smaller the primary particle size the higher the surface area, consistent with the high specific surface area, $a_{BET} = 526$ m^{2}g^{-1}, determined by N$_2$ adsorption using the Brunauer-Emmett-Teller (BET) method (Brunauer et al., 1938). Due to their slightly oxidized surface, gas blacks are acidic. Based on these characteristics, we choose FW200 soot with the goal to identify a potential laboratory surrogate for atmospherically aged soot.

LB_OEC: A lamp black carbon was obtained from OEC. Lamp black carbons generally have a broader primary particle size distribution and a lower specific surface area compared to gas black soots. In the case of LB_OEC, produced by the lamp black process, the manufacturer specifies an average primary particle sizes of $\bar{d}_{pp} = 95$ nm, comparable to the $\bar{d}_{pp} = 119$ nm we derived by TEM (see Appendix D). Soot aerosols with a wide primary particle size distribution usually result in aggregates that span a relatively wide size range compared to soots with a narrow range of primary particle sizes. At the same time, the fraction of particles containing many primary particles should be limited when selecting a mobility diameter close to the reported $\bar{d}_{pp}$. Nitrogen BET surface area was measured to be 24 m^{2}g^{-1}. Similar soot has been used for previous ice nucleation studies (DeMott et al., 1999), rendering a direct comparison of our results feasible.

LB_RC: Another amorphous lamp black soot, lamp black Rublev Colours (RC), was purchased from Natural Pigments LLC, (Willits, California, USA). It is also produced by the lamp black process and we found an average primary particle size of $\bar{d}_{pp} = 152$ nm, by evaluating TEM images. Its specific surface area was measured to be 233 m^{2}g^{-1}. This sample is directly comparable to the lamp black soot purchased from OEC, due to their very similar physical properties, thus, allowing for a direct comparison of the ice nucleation abilities of the same soot type stemming from different combustion sources.

miniCAST soot: Combustion aerosol was generated using a miniature combustion aerosol standard (miniCAST, Model: 4200, Jing Ltd., Zollikofen, Switzerland). The miniCAST produces soot aerosol in a co-flow diffusion flame, mixing two concentric, interleaved flows of propane (inner flow) and particle-free, VOC-filtered, synthetic oxidation air (outer flow). Changing the fuel-air ratio varies the properties of the resulting aerosols, such as mean aggregate size, morphology and OM content over a wide range and in a reproducible fashion (Moore et al., 2014; Schnaiter et al., 2006; Mueller et al., 2015; Mamakos et al., 2013; Yon et al., 2015). It has been shown in the past that miniCAST soot can mimic the physicochemical properties of aircraft soot (Bescond et al., 2014). Here we test two soots that differ in OM content, namely a sample termed **mCAST black** produced under fuel lean conditions, with a C:O ratio of 0.21 and $\bar{d}_{pp} = 31$ nm, as well as a more organic rich soot, termed **mCAST**

brown, with a flow C:O ratio of 0.23 and $\bar{d}_{pp} = 21$ nm. Details about the miniCAST operation conditions used here are given in Appendix C. The specific surface area using N_2 absorption was measured at $120~\mathrm{m^2g^{-1}}$ and $70~\mathrm{m^2g^{-1}}$ for mCASTblack and mCASTbrown, respectively.

FS: Lastly, FS, a fullerene soot, was purchased from Sigma Aldrich, Darmstadt, Germany. Fullerenes are hollow molecules of carbon atoms, arranged in a highly symmetric manner (Krätschmer et al., 1990). This fullerene soot mainly consist of C_{60} molecules with a minor fraction of C_{70} (see Table 1). Fullerene-like soots are often used as surrogates for particles produced by emissions from diesel engines (Muller et al., 2005). The FS investigated here had a specific surface area of $265~\mathrm{m^2g^{-1}}$ and the derived primary particle diameter was 41 nm.

Table 1. Particle characteristics of soot types investigated in this study, where $\bar{d}_{pp}$ denotes the mean physical diameter of primary particles, as obtained from TEM evaluation; $a_{BET,N2}$ the BET specific surface area using N_2 adsorption at 77 K and ML_{950} the mass loss at 950 °C measured by thermogravimetric analysis, as an upper limit of heat sensitive material associated with the soot. D_{fm} denotes the fractal dimension derived from power-law fits of the form of Eq. (B4) to mass-mobility data.

Type of soot	mCAST black	mCAST brown	FW200	LB_OEC	LB_RC	FS
Source	miniCAST[a]	miniCAST[a]	Orion Engineered Carbons Colour black FW200 powder Gas black process	Orion Engineered Carbons Flammruss FR101 powder Lamp black process	Natural Pigments LLC Lamp black process	Product no.: 572497, Lot no. MKBB8240V
Form/Dispersion method	combustion	combustion	Powder/FBG[e]	Powder/FBG[e]	Powder/FBG[e]	Powder/FBG[e]
General classification			amorphous CAS-no.: 1333-86-4	amorphous CAS-no.: 1333-86-4	amorphous CAS-no.: 1333-86-4	C_{60} (78.7 %), C_{70} (18.8 %), $>C_{70}$ (1.6 %), Fullerene oxides (0.9 %)
$\bar{d}_{pp}$ (std.) [nm]	31 (5.9)	21 (4.9)	22 (3.9); 13[b]	119 (43); 95[b]	152 (55.7); 95[f]	41 (12.9); [f]
ML_{950} °C [%]	15.62	18.58	31.43; 20[c]	0.97	2.8	33.37
$a_{BET,N2}$ [$\mathrm{m^2g^{-1}}$][d]	120	70	526	24	23 (20)	265
D_{fm} [-]	1.86	2.31	2.35	2.64	2.83	2.5
Ice nucleation studies	Möhler et al. (2005b) Crawford et al. (2011) Friedman et al. (2011)			Dymarska et al. (2006) DeMott et al. (1999)	see LB_OEC	

[a] Series 4200, see Table C1 for detailed flow settings

[b] specified by manufacturer based on ASTM (American Society for Testing and Materials) International standard D3849

[c] specified by manufacturer based on DIN 53552

[d] N_2 BET see Appendix B1

[e] aerosolized using the Fluidized Bed Aerosol Generator, Model 3400A, TSI Inc.

[f] specified by manufacturer

2.2 Experimental setup

The experimental setup can be divided into three main sections as shown in Fig. 1, namely aerosol generation, aerosol selection and ice nucleation, which are briefly described below.

Aerosol generation: Soot aerosols were generated using different techniques, as specified in Table 1. Dry-dispersion was used

for samples available in powder form through a Fluidized Bed Aerosol Generator (FBG, Model 3400A, TSI Inc.), operated with a bed flow rate of 10 Lmin^{-1}, a chain purge flow rate of 2 Lmin^{-1} along with a variable chain feed rate to achieve stable aerosol number concentrations. Particles from the FBG were subsequently passed to a 0.125 m^3 stainless steel mixing volume, equipped with a fan to keep the particles suspended. Contrary, the miniCAST soot samples, were directly generated in

5 the laboratory from the propane burner. Aerosol particles for ice nucleation experiments were sampled isokinetically from the miniCAST, using forward-pointing inlets centered at the outlet. The aerosol particles were then fed through a dilution system
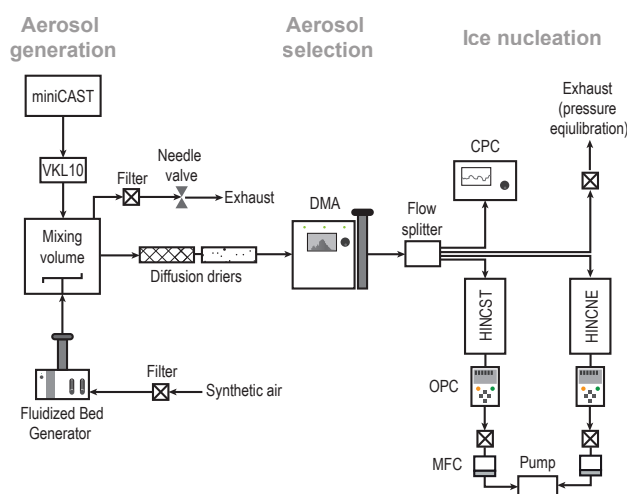
Figure 1. Schematic of the experimental setup comprising three different stages: aerosol generation, aerosol size selection and ice nucleation measurements. Arrows indicate the direction of the aerosol flow. Aerosol particles were either produced by the miniCAST burner or generated from the FBG. See text for details of instrument details and abbreviations.

(Model VKL10, Palas) using particle-free, VOC-filtered air, prior to entering the mixing volume. Combustion particles for filter collection and analysis were directly sampled from the miniCAST outlet.

Aerosol selection: From the mixing volume particles were size-selected before being sampled into HINC for ice nucleation

10 analysis. Employment of a mixing volume enhances coagulation, increasing the size of the soot aggregates and buffers any fluctuations in particle generation allowing for a constant particle number concentration during the ice nucleation experiments. From the mixing volume, particles were sent through a DMA (Differential Mobility Analyzer; Classifier 3080, with a 3081 column and a polonium radiation source, TSI Inc.), where they were size selected based on their dry electrical mobility diameter, d_{m} (see Supplementary Information (SI) Table S1 for flow settings). Downstream of the DMA, the flow was split using a

15 four-way flow splitter (Model 3708, TSI Inc.) to the various instruments, as depicted in Fig. 1. Particle number concentration was monitored using a CPC (Model 3776, TSI Inc.), operated in the low flow mode (0.3 Lmin^{-1}).

Ice nucleation: Two similar HINC chambers were connected to the flow splitter, with the last port being used for exhaust flow to avoid over-pressuring the setup. The two HINC chambers used encompass HINC*ST* and HINC*NE*, where the suffix *ST* denotes standard and *NE*, non-evaporation operation conditions, respectively. An evaporation section at the end of HINCNE

can selectively be switched on or off and HINCNE used here is identical to the chamber described in Lacher et al. (2017), i.e. not making use of the evaporation section and as such, identical to HINCST. To ensure that results obtained from both chambers are comparable, the chambers were characterized prior to the soot experiments using aerosols with thermodynamically well defined ice formation properties and good agreement was found within instrumental uncertainty (see SI Fig. S16). For

5 this reason, we generally refer to both instruments as HINC in the following and combine their data for our analysis. To avoid external contamination from entering the setup, the system was run with an over-pressure from the aerosol generation source to the splitter. The over-pressure was regulated with a needle-valve controlled exhaust, mounted to the mixing volume. This was possible as the total flow from the aerosol generation was approximately 12 Lmin^{-1} in case of the FBG and 35 Lmin^{-1} in case of the miniCAST.

2.3 Ice nucleation experiments and data processing

Ice nucleation experiments with HINC were conducted in deposition and/or condensation mode between 218 K and 253 K, in 5 K steps. HINC is a continuous flow diffusion chamber (Rogers, 1988; Rogers et al., 1998), based on the design of the UT-CFDC (University of Toronto Continuous Diffusion Chamber; Kanji and Abbatt, 2009) and is described in detail by Lacher

15 et al. (2017). Briefly, two parallel, horizontally oriented copper plates separated by a 20 mm polyviniylidene fluoride (PVDF; Angst+Pfister AG, Zurich, Switzerland) spacer are lined with borosilicate glass fiber filter paper (Type A/C, Pall Corporation) which is wetted prior to cooling. Upon cooling of the walls (copper plates) to subzero temperatures, a smooth ice layer is formed on the wetted filter paper. The wall temperatures are controlled by two thermostats (LAUDA ProLine RP890C) to keep temperature fluctuations around 0.1 K and are monitored through four equally spaced thermocouples along each wall. When

20 held at different temperatures, a linear temperature gradient is established between the upper (relatively warmer) and lower (relatively colder) wall, resulting in a parabolic water vapor supersaturation profile across the chamber, due to the nonlinear relationship between saturation vapor pressure and temperature (Clausius-Clapeyron equation). Cloud particles can be formed within the chamber by exposing the injected aerosol particles to RH conditions $RH_i > 100$ %, where the subscript *i* denotes evaluation with respect to ice. Freezing experiments with salt particles have been performed and compared to theoretical

25 predictions from the water activity based homogeneous freezing parametrization of solution droplets (Koop et al., 2000) to verify chamber performance (Lacher et al., 2017). The flow in HINC is maintained by two mass flow controllers (MFC, G-Series, MKS Instruments, Andover, USA), which control the sheath air and total flow. The sheath air flow (F_{sheath}) is made up of particle-free N_2 and confines sampled particles to a lamina at the center of the two walls, corresponding to a specific temperature and RH while preventing interaction of the particles with the walls. The total flow through HINC (F_{OPC}) denotes

30 the flow that is sampled by the optical particle counter at the chamber outlet. The aerosol containing sample flow (F_{AP}), drawn into HINC, is given by the difference of F_{OPC} and F_{sheath}. The aerosol flow was chosen such that the ratio of F_{AP} to F_{sheath} was between 1:10-1:12, by adjusting F_{sheath} and keeping F_{OPC} fixed at 2.83 Lmin^{-1}. The particle residence time within HINC is purely a function of the position of the movable injector as described by Lacher et al. (2017), for a constant total flow (F_{OPC}). Assuming a perfectly parabolic velocity profile across the chamber, the aerosol particles are assumed to travel at the

maximal velocity at the centre of the profile, which is used to derive the particle residence time in the chamber. The residence time is the sum of a nucleation and water droplet or ice crystal growth time in the chamber. For all experiments presented here a particle residence time of $\tau \approx 16$ s was chosen, allowing the nucleated ice crystals to grow to sizes of a couple of micrometers in diameter within the chamber. At the HINC outlet, an optical particle counter (OPC, Model GT-526S, MetOne) is used to

5   detect particles. The OPC can count and size particles in the size range between 0.3 μm and 10 μm (optical diameter) and can be operated at six different, customizable size bins within this range. However, it does not have phase discrimination capability, as such discrimination between interstitial aerosol particles, cloud droplets and ice crystals is based purely on optical particle size. Here, we choose the 1 μm size bin as the threshold to detect ice crystals in HINC, i.e. particles with optical diameters > 1 μm. This threshold size was set above the size of aerosol particles entering HINC but small enough to capture the onset

10   of ice formation. Conditions at which water droplets grow to sizes larger to the ice crystal threshold size is referred to as water droplet survival (WDS) relative humidity and is a function of T, initial aerosol size and residence time in the chamber. Beyond that size (bin) ice crystals and cloud droplets cannot be distinguished any longer. Water droplet growth was calculated assuming pure diffusional growth based on Rogers and Yau (1989) for a given initial diameter corresponding to the size of the selected aerosol, and assuming the entire residence time within HINC is available for diffusional growth, i.e. neglecting

15   any nucleation time. Therefore, the calculated values represent an upper limit of droplet growth and thus a lower limit of the WDS relative humidity reported. In our case the WDS line is only slightly above water saturation due to the 1 μm OPC channel used to report ice nucleation (see Fig. 2). Data points occurring above the WDS line are not considered to represent heterogeneous ice nucleation. Nevertheless, we cannot exclude that heterogeneous ice formation takes place simultaneously with or after droplet formation. For all experiments the OPC was operated at a logging interval of 5 s, such that the detected

20   counts within a given size channel yield the cumulative counts detected during this period. While most of the samples were probed using the six channel MetOne OPC, some experiments were performed using a four channel LightHouse OPC (Model R3014) during instrument unavailability. However, the same settings and analyses were applied to ensure consistency in data treatment and comparable results. Ice nucleation abilities of the soot aerosol were probed by so-called RH ramps where the aerosol is exposed to increasing RH at fixed T. To achieve this, the desired lamina (center) temperature is set and then the

25   RH is increased by cooling and warming the temperatures of the two walls at the same rates. Instrumental noise from HINC, including occasional frost particle detection, was determined with a particle-free flow in HINC at the beginning and the end of each RH scan. The background counts, corresponding to a linear interpolation of the OPC counts detected during the particle-free periods, were subtracted from the data and all of our reported values are above this background level, as described in detail in Lacher et al. (2017).

30   The fraction of aerosol particles that nucleated ice is called the activated fraction (AF), defined as the ratio of the number concentration of ice particles detected by the OPC in the 1 μm size channel, $n_{ice,CH1\mu m}$, to the total number concentration of particles entering the chamber, n_{tot}, as determined by the CPC in parallel to HINC:

$$AF = \frac{n_{ice,CH1\mu m}}{n_{tot}}. \tag{1}$$

The uncertainty range in AF is ±14 %, resulting from a 10 % counting uncertainty in each of the OPC and CPC. The fractal-like nature of soot aggregates causes the structure of monodisperse aerosols to vary on a particle to particle basis (Park et al., 2004), affecting aerosol properties such as shape and surface area thus adding to the complexity when size-selecting soot aggregates. This resulted in larger aerosol particles (optical diameter > 1 μm) being detected in the ice channel making it necessary to aerosol-correct some of the AF curves, when evaluating the 1 μm OPC channel. Finally, all ice nucleation results presented below correspond to mean AF values observed over a range of two to eight RH scans performed at a given temperature. We constrained the ramp rate of our RH scans to below 3 %min^{-1}, evaluating RH with respect to water. The CFDC data was then linearly interpolated into bins of 0.25 % RH_{w}, where the subscript w denotes evaluation with respect to water. Thus, each reported curve represents the arithmetic mean of all binned and interpolated RH_{w} scans performed at a given temperature for a given soot sample.

2.4 Auxillary measurement for sample characterization

A suite of auxiliary measurements were conducted to characterize the physicochemical properties of the tested soots, which ultimately aid in determining their ice nucleation behavior. Details of the measurements can be found in Appendix B and are briefly described in the following. The fractal extent of the soot aggregates was determined through TEM and coupled DMA-CPMA (Centrifugal Particle Mass Analyzer, Cambustion Ltd., Cambridge, UK) measurements to assess the fractal nature of the soots. In addition, all soot types were investigated by means of a thermogravimetric analyzer (TGA; Model Pyris 1 TGA, PerkinElmer) to determine the particle fraction that can be volatilized as a function of temperature, referred to hereafter as the mass loss at a given temperature. This was done to determine the presence of any secondary material coating the carbon spherules of the soot aggregates. In order to determine the hydrophilicity and infer the porosity of the samples, gravimetric water vapor sorption isotherms of the soot particles were measured by Dynamic Vapor Sorption (DVS, Model Advantage ET 1, Surface Measurement Systems Ltd., London, UK). Finally, the BET specific surface area of the samples was determined from additional N$_2$ adsorption measurements ($a_{BET,N2}$). The $a_{BET,N2}$ values were used in combination with the water sorption measurements to derive equivalent water monolayer coverage.

3 Results and discussion

3.1 Overview of ice nucleation measurements

An overview of the ice nucleation experiments is given in Fig. 2. From this overview a few key features are inferred concerning the ice nucleation ability of the tested soot particles. A clear dependence of ice nucleation of soot on the temperature regime can be identified. For $T > 235$ K all soot types require water saturation for activation into ice crystals and/or cloud droplets. The fact that the activation onset conditions for all soot types (independent of particle size) lie at $RH_{\mathrm{w}} \geq$ WDS (dashed blue line in Fig. 2), indicates an absence of heterogeneous freezing for $RH_{\mathrm{w}} <$ WDS. However, we re-iterate that we cannot unambiguously distinguish between cloud droplets and ice crystals at $RH_{\mathrm{w}} \geq$ WDS, given that cloud droplets can grow to
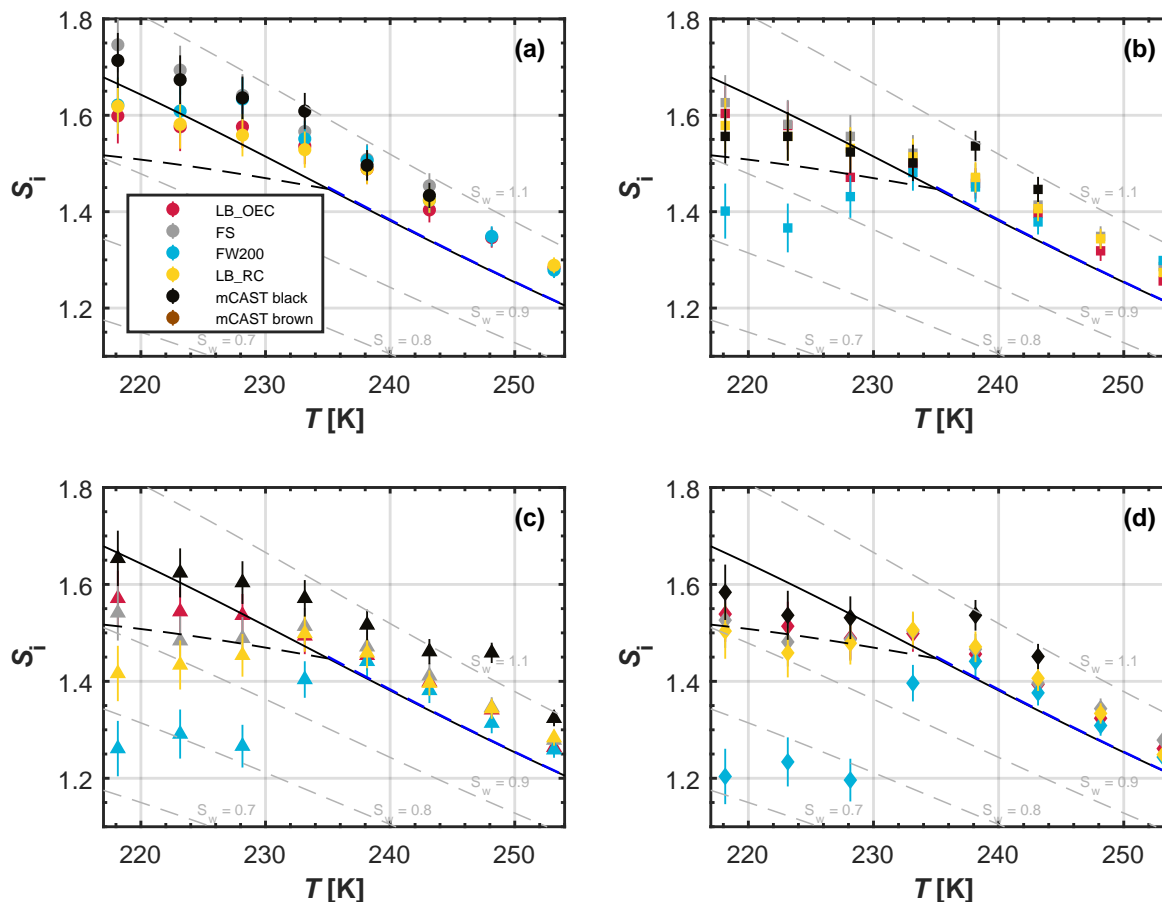
Figure 2. Onset saturation ratio with respect to ice (S_i) of freezing where 1% of the aerosol particles are activated as a function of temperature for (a) 100, (b) 200 (c) 300 and (d) 400 nm size-selected particles. The black, solid lines denote water saturation using the water saturation pressure parameterization given by Murphy and Koop (2005); gray, dashed lines indicate offsets from this line in steps of 0.1 to guide the eye. The black, dashed lines mark the homogeneous freezing threshold for supercooled solution droplets according to Koop et al. (2000). The blue dashed line indicates WDS conditions. WDS appears close to water saturation for the 1 μm OPC channel used. Each dot represents the mean of a minimum of two RH-scans performed with HINC. Temperature uncertainty is 0.1 K and S_i uncertainties, outlined in Appendix E1, are indicated as vertical bars. We note that mCAST black and brown do not activate to 1% and are thus not plotted for some conditions (see SI Sect. S2 for complete AF curves).

1 μm by water vapor diffusion and be detected as ice crystals. Furthermore, evaluating the ice nucleation data for the 5 μm OPC channel, where WDS is well above water saturation for the residence time of $\tau \approx 16$ s, reveals that activation onset only takes place for $RH_w \geq$ WDS (see SI Sect. S3). Thus, we can conclude that no condensation/immersion freezing of soot takes place in the region $100\% < RH_w <$ WDS for the MPC temperature regime. This interpretation is consistent with Koehler et al. (2009), who did not find ice nucleation at temperatures above 233 K. Conversely, in the cirrus temperature regime some

soot particles nucleate ice below homogeneous freezing conditions. From this, we conclude that the unprocessed soot types investigated here can significantly contribute to ice nucleation only in the cirrus regime.

A strong increase in the freezing ability below the homogeneous nucleation temperature (HNT, 235 K) has been observed before for kaolinite (Welti et al., 2014) and suggests the involvement of a liquid water phase in the ice formation process,

5 similar to the soot particles tested here.

Moreover, a clear size dependence is observed, with larger soot aggregates showing activation at lower RH at a given temperature. A size dependence is consistent with the INP requirements reported in Pruppacher and Klett (1997) proposing that INP typically have (physical) diameters ≥ 200 nm. While these findings are confirmed by more recent studies for mineral dust (e.g. Archuleta et al., 2005; Welti et al., 2009), ice nucleation measurements of size selected (e.g. Friedman et al., 2011; Kulkarni

10 et al., 2016) or nearly monodisperse soot particles (DeMott, 1990) are limited, especially in the cirrus regime. The observation that the 100 nm soot particles only induced ice formation above homogeneous freezing conditions, suggests that particles of this size are not relevant for forming ice crystals at $T < 233$ K, irrespective of morphology and composition since homogeneous freezing of droplets will out-compete any heterogeneous nucleation by soot particles in the cirrus temperature regime. Besides a dependence on the minimum aerosol size, ice nucleation has been suggested to depend on the chemical composition

15 of the INP (Pruppacher and Klett, 1997). This is consistent with our results, which only show differing ice nucleation abilities among the soot types for particles with sizes of 200 nm or larger tested here. Nevertheless, the absence of freezing of our 100 nm soot particles, at conditions below homogeneous freezing of solution droplets reveals that both particle size and chemical properties determine the ice nucleation ability of the investigated soots. To further elucidate which properties provide soots with ice nucleation activity, we focus here on the ice nucleation results of the most active 400 nm particles in the cirrus regime.

20 We show the complete activation curves in Fig. 3, in order to discuss differences in the ice nucleation mechanisms associated with the soot types with information gained from the auxiliary measurements performed on the soot samples.

3.2 Ice nucleation dependency on soot type

Figure 3 shows the AF as a function of RH_w for all investigated 400 nm soot samples, covering the temperature range $218 - 233$ K. Given that the RH_w range between homogeneous freezing condition and water saturation at $T = 233$ K spans

25 only approximately2 % RH_w, which is within our instrumental uncertainty, we cannot exclude that water saturation conditions were reached for the observed freezing at 233 K. Overall, soot particles require high ice supersaturations to nucleate ice, rendering them unlikely to contribute to heterogeneous freezing at $T = 233$ K within the residence time of HINC. An exception is FW200, which shows activation well below homogeneous freezing conditions for all temperatures shown in Fig. 3. This becomes more apparent at lower temperatures. At $T = 218$ K FW200 shows significant freezing at RH as low as $RH_w = 70$

30 %. This heterogeneous freezing ability of FW200 is even more pronounced than that found by Koehler et al. (2009), who reported AF of roughly 1 % below homogeneous freezing conditions, when testing thermal oxidized soot, i.e. soot processed in a mixture of nitric and sulfuric acid, at $T = 233$ K. The lower ice nucleation onset of FW200 soot can be interpreted as a more active deposition nucleation process due to the larger surface area of the FW200 compared to the other soots (see Tables 1 and B1). However, the absence of ice nucleation below water saturation for $T > 233$ K is incompatible with a classical
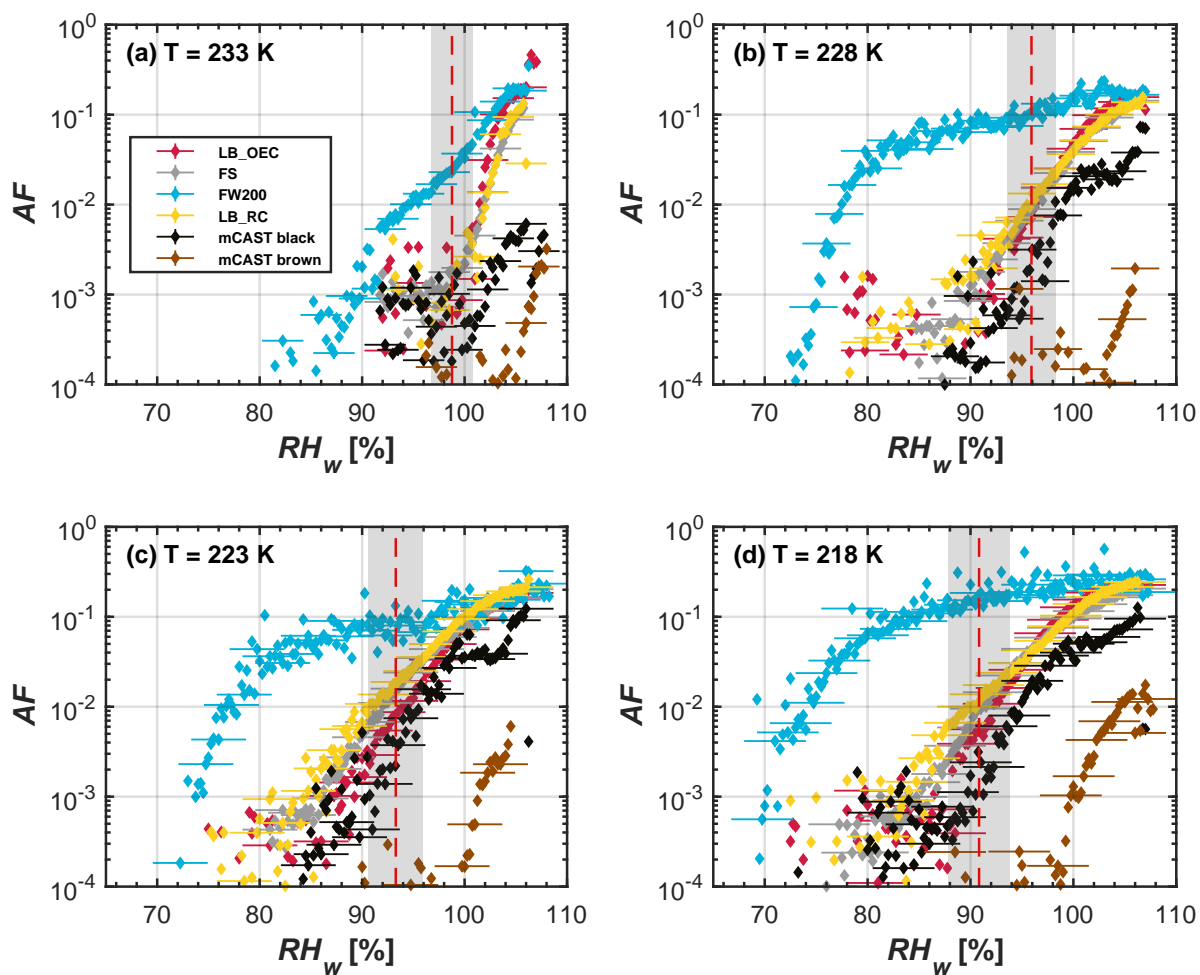
Figure 3. Mean RH scans of 400 nm mobility diameter soot particles, showing AF as a function of RH_w for different temperatures in the cirrus regime. Red dashed lines represent expected homogeneous freezing conditions according to Koop et al. (2000), and the gray shaded regions indicates the calculated RH_w variation across the aerosol lamina in HINC. Uncertainties, given for every 5th data point, are as in Fig. 2.

deposition nucleation (Welti et al., 2014). As mentioned above, the dependence on the HNT supports the interpretation that liquid water is involved in the freezing mechanism prior to reaching water saturation. This suggests a homogeneous freezing mechanism for the FW200 particles below water saturation. Soot aerosols typically consist of agglomerated chains of spherical particles they are prone to form cavities and/or pore-like features between the primary spherules and the individual chains, in which water can condense at water subsaturated conditions (inverse Kelvin effect, Marcolli, 2014), and can subsequently freeze homogeneously through a so-called pore condensation and freezing mechanism (Higuchi and Fukuta, 1966; Fukuta,

1966; Christenson, 2013; Marcolli, 2014). During PCF, water that is taken up in capillaries well below water saturation, can freeze homogeneously if the temperature is below the HNT and if the pore diameter is large enough to accommodate the critical ice germ. Freezing of pore water can subsequently trigger macroscopic ice growth, resulting in ice crystal formation. The steepness of the activation curves for FW200 shown in Fig. 3 resemble a step-like activation when reaching a critical

5   RH, consistent with a PCF type mechanism which requires the pores on the soot aggregate to fill and subsequently freeze homogeneously. In fact, the large specific surface area of FW200 itself (see Table 1 and B1), must be caused by concave and convex surfaces formed from the sintered primary particles and potentially indicates the presence of cavities. Additionally, aggregate porosity in the form of voids formed between sintered primary particles is supported by our TEM analysis (see Sect. 3.3). Yet, we note that none of the other soots tested shows a similarly clear ice nucleation behavior attributable to PCF. Thus,

10   the observed difference must be related to the physical and chemical properties of the particles. We discuss these in the context of possible different freezing mechanisms between the soots in the following.

3.3   Soot particle fractal structure

Soot morphology was derived from DMA-CPMA measurements (see Appendix B4), and qualitatively from analysis of TEM images (see Appendix D). The fractal dimensions, D_{fm}, of the different soot types are reported in Table 1 and the corresponding

15   DMA-CPMA data is shown in Fig. 4. A D_{fm} value of 1 corresponds to a straight chain-like structure, whereas $D_{\text{fm}} = 3$ indicates a compact sphere like structure. In general the values of the fractal dimensions lie within those observed in previous studies, such as the values reported for Diesel soot by Olfert et al. (2007), ranging from 2.2 to 2.9, or Abegglen et al. (2015), who observed values from 1.86 to 2.88 for particulate matter from aircraft turbine exhaust. Our DMA-CPMA measurements reveal a similar mean fractal structure of the different soot types. However, we cannot identify a direct relationship of the fractal

20   dimension to the ice nucleation efficiency of the soot types reported in Fig. 3 above.

     Interestingly, the two lamp black soots (LB_OEC and LB_RC) show significantly higher masses for a given mobility diameter compared to the other soots. The higher mass for a selected size of the lamp black soots translates into larger effective densities for these soots, given as median particle mass divided by the equivalent volume of a sphere with this mobility diameter. From our TGA mesurements we can exclude the contribution of secondary material to cause the higher masses of the

25   lamp black soots (see Sect. 3.4). The higher masses for the lamp black soots are more likely caused by larger primary particles making up these aggregates resulting from the wider size distribution of the primary particles. As noted above, the lamp black soots have a rather wide primary particle size distribution, causing the resulting soot aggregates to be composed of primary particles with different masses. This is also reflected in the relatively larger error bars of the lamp black soots in Fig. 4 and further supported by our TEM analysis.

30   In general our TEM results reveal large, fractal like aggregates composed of primary particles that form a variety of different micro structures. In Fig. 5 we show exemplary TEM images of the different soot types for $400\ \text{nm}$ size selected aggregates (see also SI Fig. S18). Images of both the LB_RC and LB_OEC reveal a range of differently sized primary particles making up the aggregates. This is further supported by the size distribution of primary particles shown in SI Fig. S17, for which a larger number of aggregates and primary particles has been evaluated. From the TEM images depicted in Fig. 5 we further note that
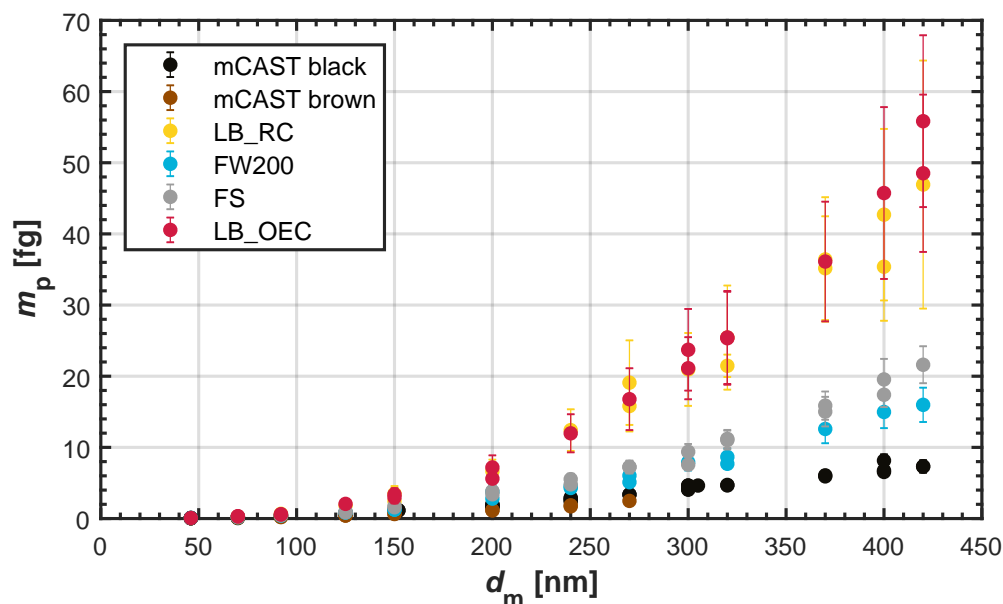
Figure 4. DMA-CPMA data for the different soot types: Electrical mobility diameter (d_m) vs. median particle mass (m_p) derived from fitting the resulting mass distribution with a log normal distribution. Error bars correspond to standard deviations of the individual measurements.

the most ice active FW200 soot shows particularly densely clustered aggregates, whereas the other soots exhibit more branched, chain-like aggregates. It should be noted that these TEM images constitute only a 2D projection of the soot aggregates and can thus not be directly compared with the 3D fractal dimension derived from our CPMA-DMA measurements. We conclude from our TEM analysis that all soot types demonstrate aggregate structures that encompass cavities and pores, which could enable a

5 PCF freezing mechanism. Nevertheless, it is likely that the clear difference in primary particle size determines and/or strongly influences overall aggregate porosity. Soot aggregates of a given mobility size are composed of an increasing number of carbon spherules for decreasing primary particle sizes. As the number of spherules increases the propensity for pores in an aggregate also increases due to the potential for pores between sintered spherules and/or through intra-aggregate cavities between the branches of the aggregate. As such, soot particles with smaller spherules are more likely to nucleate ice via a PCF mechanism

10 due to the higher concentration of pores. Indeed, a recent study by David et al. (in prep.b) showed that macroscopic ice can only grow out of cylindrical pores if they are closely spaced. Therefore, it is possible that the enhanced ice nucleation capabilities of FW200 are caused by its small spherule size and the associated increased propensity for pores. However, it is important to note that the mCAST brown soot shows a similar spherule size distribution to the FW200 soot, but also a significantly more branched 2D projection of the aggregate and exhibits significantly lower ice nucleation ability compared to FW200 soot. Thus,

15 the observed difference must be related to other physical and chemical properties of the particles, in addition to the morphology. Next we discuss the presence of volatile material on the soot particles.
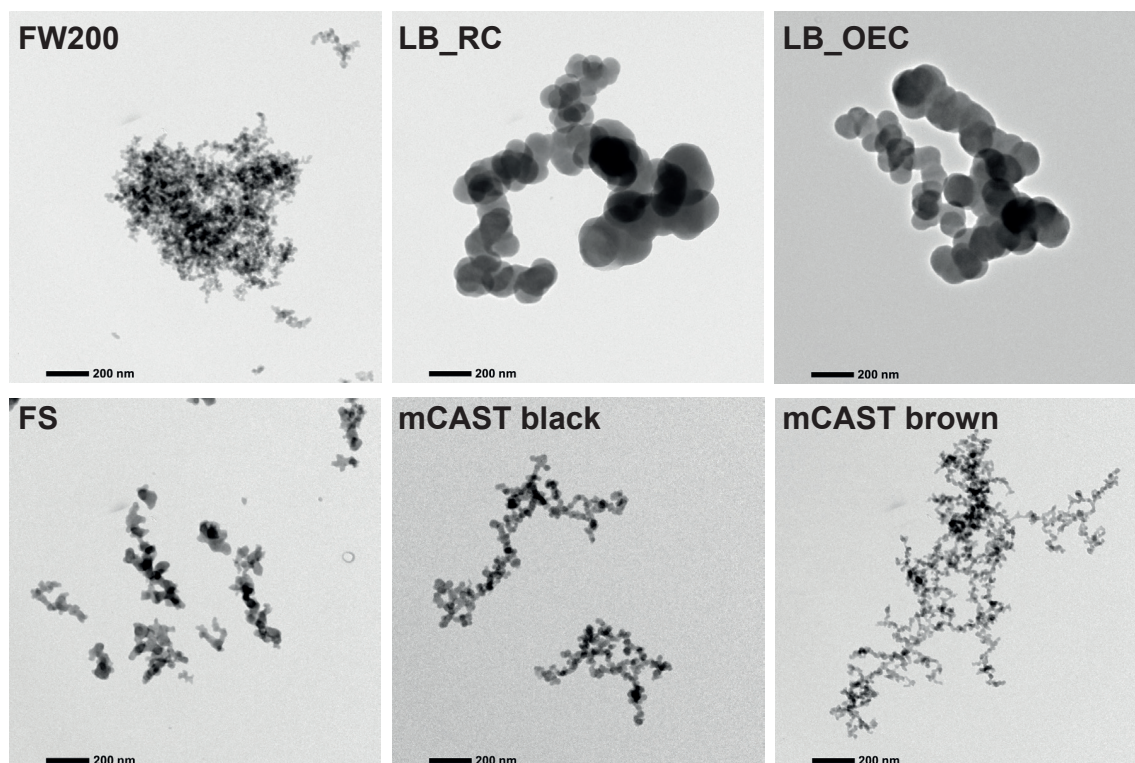
Figure 5. Exemplary TEM images of representative soot aggregates of the different soot types when selecting 400 nm mobility diameter particles with the DMA.

3.4 Temperature dependent mass loss

Besides carbon, soots usually contain OM which can include compounds with hydrophilic functional groups such as hydroxyls, carbonyls or carboxyls. Heating the soot samples leads to the loss of this OM, depending on the heat resistance of the compounds. A loss in mass encompasses the volatilization of associated OM and/or the thermal decomposition of OM at higher temperatures. The mass loss of the soots as a function of T, measured by TGA, is shown in Fig. 6. Here we focus on the mass decrease within three different temperature regimes (color shading in Fig. 6).

 Highly volatile compounds, classified as volatile at temperatures below 200 °C, evaporate under inert gas flow (yellow shading in Fig. 6). In the range below 100 °C FW200 shows the strongest reduction of mass of approximately 7 % (7.5 % and 6.5 % for samples with solid and dashed lines, respectively). We interpret the strong decrease in mass of FW200 to be caused by the loss of adsorbed/condensed water and/or low molecular weight organic substances. The observed mass decrease of approximately 9 %, when drying the FW200 sample for 1000 min at 25 °C by continuous N_2 flushing prior to the DVS measurement, supports the interpretation that the mass loss is due to evaporation of water (see SI Fig. S14). Besides, the mass loss rate is highest below 100 °C, likely due to evaporation of adsorbed water vapor and stays approximately constant between
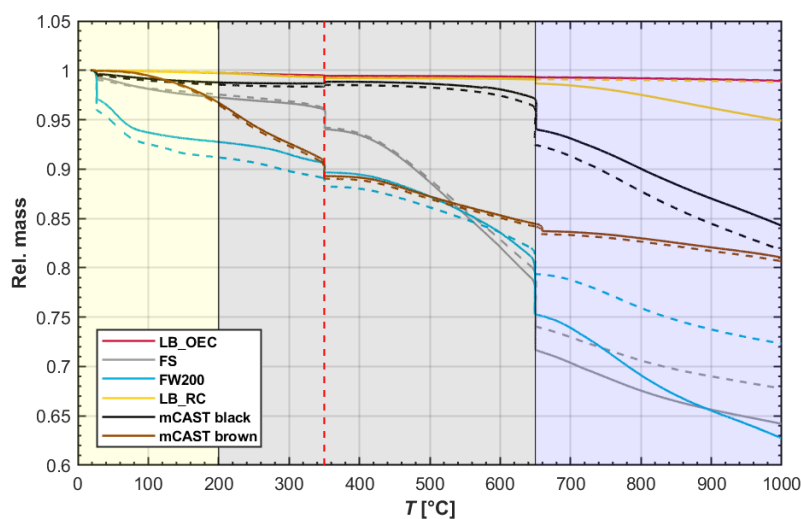
Figure 6. Results of the TGA analysis of the investigated soot types in a nitrogen atmosphere, showing the relative sample mass as a function of sample temperature. Solid and dashed lines indicate the results of two individual TGA runs. Shadings correspond to different ranges of volatilization, namely adsorbed water and highly heat sensitive material (yellow), medium heat sensitive material (gray) and low heat sensitive material (blue). Pyrolysis is expected to contribute to mass loss at temperatures above the vertical red dashed line.

100 °C and 400 °C (see SI Fig. S13). Overall, the strong mass decrease of FW200 below 200 °C may reflect the presence of strongly hydrophilic sites on this sample, where moisture can adsorb. The high affinity of FW200 to adsorb water is further reflected by the DVS experiments (see Sect. 3.5). In contrast, the equivalent mass loss for the mCAST black and the lamp black soots is significantly lower, measured as less than 1 % up to temperatures of 100 °C. A water content of at most 1 %

5 indicates only a limited number of hydrophilic active sites or pores where water can be adsorbed. While most soot types show strong mass loss below $T = 100$ °C the mass of mCAST brown is relatively constant within this temperature range but then decreases for temperatures between approximately 140 °C and 200 °C. Up to $T = 200$ °C the mass loss of the mCAST brown soot is likely associated with highly volatile, low molecular mass polyaromatic hydrocarbons (PAH), that have previously been associated with brown carbon from the miniCAST burner (Mueller et al., 2015) and which have been reported to volatilize

10 between approximately 100 °C and 200 °C (Portet-Koltalo and Machour, 2013). Conversely, the mCAST black samples show a smaller mass reduction, indicating a lower proportion of volatile OM, illustrating the chemical difference to the mCAST brown sample. The increased OM content on brown carbon results from a reduced combustion temperature and a less complete combustion compared to mCAST black as a consequence of an increased amount of N_2 premixed to the fuel for this test point (see Appendix C). This supports the interpretation from above that the mass loss observed for mCAST brown is mainly due

15 to OM and not due to sorbed water vapor, which above $T = 100$ °C should have already been desorbed. The lack of sorbed water also suggests that the OM is likely hydrophobic in nature. Considering our ice nucleation results reported in Fig. 3, the shift of the onset of mCAST brown to higher supersaturation compared to the mCAST black (and the other soots) suggests that

these hydrophobic hydrocarbons suppress the freezing abilities of the soot. This interpretation is in agreement with the results from Crawford et al. (2011) and Möhler et al. (2005b) who find freezing for propane soots with higher organic carbon content required higher supersaturation for ice nucleation.

The FS sample demonstrates a strong mass loss above 350 °C, indicating a relatively large abundance of material with medium volatility compared to the other soots. While some portion of this mass loss is attributable to OM with medium volatility (see Fig. 5), it is likely that thermal decomposition in the form of pyrolysis also contributes to mass loss (Bredin et al., 2011; Song and Peng, 2010). Besides, we cannot exclude combustion of carbon in the presence of trace amounts of oxygen (trapped within the sample, instrument parts or from gas impurities), which has been shown to contribute to mass loss between $430 - 650$ °C, even for N_2 prepurged samples. Bredin et al. (2011) found combustion (in the presence of oxygen) contributing to a mass change of a Printex U soot (gas black) in TGA measurements performed in a N_2 atmosphere. They reported combustion starting around 400 °C and reaching a maximum rate around approximately 500 °C, similar to the behavior of our FS soot. In conclusion, both pyrolysis and combustion can occur in this temperature range, depending on the presence of O_2 in the reaction chamber. The consistent mass loss in this temperature range for both independent TGA runs with FS (solid and dashed line), combined with the negligible mass loss of the lamp blacks and the mCAST black in this temperature range, suggests that most of the mass loss is caused by the evaporation of low-medium volatility OM. For mCAST brown, this likely includes larger, higher molecular weight PAHs which have been reported to volatilize between approximately 125 °C and 670 °C (Wang et al., 2012). If the observed mass loss of the FS aggregates was due to water-soluble material, this material could take up water and lead to the formation of aqueous solution droplets which subsequently freeze homogeneously. This process could account for the freezing reported in Fig. 2, however the lack of any change in the slope in the AF curves of FS at homogeneous freezing conditions (see SI Fig. S16) render this interpretation unlikely.

Around 400 °C the organic fraction should be completely vaporized and desorbed (Stratakis and Stamatelos, 2003). Thus soot samples which exhibit a strong mass loss beyond this temperature, namely FS, FW200, mCAST brown and to some extent also mCAST black, undergo continuous pyrolysis or contain inorganic heat sensitive material.

Altogether, TGA analysis confirms that mCAST black and the lamp blacks can be considered as pure carbons, with minimal impurities in the form of OM, while it illustrates the presence of organic material on the mCAST brown and on the FS. Overall the only sample that shows a significant mass loss for $T < 100$ °C (likely adsorbed or condensed water) is FW200, which corroborates its high ice nucleation ability compared to all the soot samples investigated.

3.5 The role of soot-water vapor interaction

An important parameter for the ice nucleation ability of the different soot types is their potential to take up water (Dubinin, 1980). The water uptake capacity is controlled by both the soot morphology (surface area and microstructure, Dubinin and Stoeckli, 1980) and the chemical composition, i.e. the availability of soluble material on the soot surface and/or the presence of hydrophilic functional groups, such as carboxyl, carbonyl and hydroxyl groups (Ferry et al., 2002). We used DVS to measure the water vapor sorption and desorption isotherms of the soots, allowing to infer of particle porosity and hydrophilicity at the same time. Figure 7 shows an overview of the water uptake of the different soots, measured by DVS at $T = 298$ K and
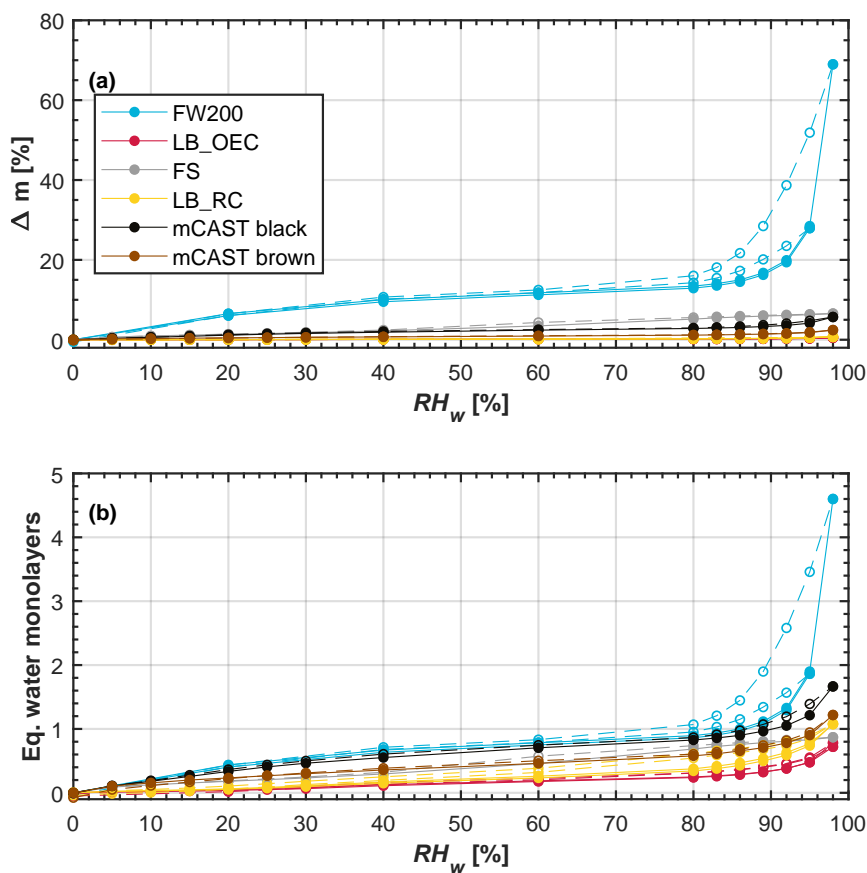
Figure 7. Water uptake (solid lines, filled symbols) and loss (dashed lines, open symbols) isotherms, given as (a) relative sample mass change and (b) equivalent water monolayers, as a function of RH_w, as measured by DVS at $T = 298$ °C. Each set of curves corresponds to an individual, independent soot sample. The data points represent water uptake/loss at quasi-equilibrated RH_w conditions. Each soot type was probed for two independent experiments in the DVS and the curves of the two independent runs lie on top of each other. Exceptions are the mCAST samples, which were only probed once in the DVS. Curves are linear interpolations between quasi-equilibrated sample points to guide the eye. The curves of the LB_OEC and LB_RC samples lie on top of each other in panel (a). All experiments were performed to a maximum RH_w of 98 %, with the exception of one FW200 sample showing a maximum relative mass change of approximately 30 %, which was only probed up to $RH_w = 95$ %.

covering the range of $0-98$ % RH_w. The water uptake is calculated from gravimetric data, expressed in percent as relative mass change difference between the initial dry mass and the quasi-equilibrated, moist sample mass at the probed RH (Fig. 7a), and expressed in terms of equivalent adsorbed water monolayers (Fig. 7b). We use the term *water uptake* to encompass both effects of adsorption and absorption. Adsorption describes the enrichment of water molecules on the solid soot surface through binding

5   of water molecules to hydrophilic sites and the formation of water molecule clusters or equivalent monolayers. Absorption, on the other hand, refers to water molecules dissolving into soluble material associated with the particles (Popovicheva et al.,

2008; Thommes et al., 2015). In Fig. 7, water uptake curves are shown by solid lines along with filled symbols, whereas water loss curves are shown by dashed lines and open symbols. Each set of (uptake/loss) curves corresponds to an individual, independent experiment, using a fresh sample of the corresponding soot type.

The uptake curves of FW200 soot rise strongly at low RH ($RH_w \leq 20$ %), exhibiting a convex shape, followed by a a slow

5   rise at intermediate RH (20 % $\leq RH_w \leq 80$ %), and a sharp increase in water mass taken up at high RH (≥ 80 %), typical for a type IV(a) isotherm (following classification recommendations according to IUPAC, see Sing et al., 1985; Thommes et al., 2015). In the FW200 aggregates water is initially taken up by *equivalent* monolayer adsorption on the soot surface (see Fig. 7b). The increase in mass at higher RH marks the transition to multilayer adsorption followed by the transition to capillary (pore) condensation at $RH_w \geq 89$ %, signified by the sudden rise in mass. This is particularly clear from the FW200 sample

10 probed until a maximum value of $RH_w = 98$ % (water uptake curve with maximum mass change $\Delta m_{max} \approx 70$ % in Fig. 7a). Due to the strong mass increase of the FW200 soot when probed until $RH_w = 98$ % and the long time scales required to equilibrate the sample at these high RH (around 800 min) we restricted further measurements of FW200 to $RH_w = 95$ %. However, all other soots were tested up to $RH_w = 98$ %. We attribute this strong water uptake at high RH_w to mesopores ($2 - 50$ nm, IUPAC, Thommes et al., 2015) formed by inter-particle cavities of the soot aggregates which create the porous

15 structure of soot already discussed above (see Sect. 3.3). The high water affinity of FW200 revealed by the DVS measurements is consistent with the observed ice nucleation at relatively low ice supersaturations. We interpret this as a low soot-water contact angle for this sample. Besides, the availability of mesopores inferred from DVS supports our hypothesis that the mechanism of ice formation on the FW200 soot is indeed PCF.

This further corroborates our discussion above that the mass loss of FW200 observed in the TGA at temperatures $T \leq 100$

20 °C is associated with desorbing water. Water uptake by OM could also contribute to the mass increase observed in our DVS experiments. Taking citric acid (CA) and glutaric acid (GA) as surrogates for typical atmospheric organics and using the mass growth factors reported in Zardini et al. (2008), we find a mass fraction of 13.6 % and 20 %, respectively, to be required to explain the observed mass change of almost 30 % at $RH_w = 95$ %. However, our TGA results only indicate a mass change of approximately 8 % and 10 % at the boiling points of CA (310 °C) and GA (200 °C, see Fig. 6). Thus, we confidently

25 attribute the water uptake of FW200 to pores present on the soot aggregates, and not only due to absorption of water vapor by hydrophilic OM.

The water uptake on FW200 is associated with a hysteresis as the water uptake and loss curves do not overlap over the complete RH range. The presence of a hysteresis loop further indicates that the mechanism of water uptake cannot be attributed to absorption by hygroscopic OM, but is indeed caused by the availability of pores and capillary condensation. The form of the

30 hysteresis loop can be used to infer information on the pore structure. For the FW200 sample probed until a maximum RH of $RH_w = 98$ % the hysteresis looks like a H3-type hysteresis loop that is relatively narrow, where adsorption and desorption curves are almost parallel (Thommes et al., 2015), but associated with a very steep desorption branch. In contrast, the FW200 sample probed until $RH_w = 95$ % ($\Delta m_{max} \approx 30$ % in Fig. 7a) resembles an H4-type hysteresis with a shallow hysteresis loop, observed for aggregated, non-rigid particles such as mesoporous soots (Thommes et al., 2015). Contrary to typical H3

35 or H4-type hysteresis loops, the FW200 soot shows hysteresis down to very low RH_w, reflecting that either micropores are

developed or present to some extent on FW200 or that some water vapor is taken up through chemisorption on active sites of the OM. While most of the hysteresis values of the FW200 soot lie within the DVS uncertainty of approximately $\Delta m = 0.75$ %, micropore filling is supported by the values of the C constant in the classical BET equation, describing the adsorbate-adsorbent interaction strength. The C-value of FW200 was found to be > 650 (see Table B1), indicating filling of narrow micropores

5 (Thommes et al., 2015). The shape of the hysteresis loop indicates involvement of mainly conical and slit-like pores as the majority of the water is lost already at high RH_w. Pores with narrow necks, so-called ink-bottle shaped pores, which remain filled during desorption until low RH (Kittaka et al., 2011), would cause a much stronger hysteresis at lower RH_w and are thus likely absent. This is consistent with the different hysteresis types, namely H3 and H4, associated with the FW200 probed up to different maximal RH_w. The H3 hysteresis loop indicates *narrow* slit-like pores formed through sintering of carbon spherules.

10 The H4 hysteresis includes also (normal) slit like pores formed in between spherules that are not adjacent (but positioned along different branches of the soot aggregate, see Fig. 5). From these observations we conclude that particle morphology and contact angle determine the water uptake by soot particles, confirming a PCF mechanism for the observed ice nucleation on FW200. This interpretation is also consistent with the observed ice nucleation onsets reported in Fig. 2. Therefore, our interpretation that the mass loss of FW200 during the TGA analysis is consistent with the evaporation of adsorbed water vapor and that the

15 ice nucleation proceeds via a PCF mechanism can further explain the difference in freezing behavior between FW200 and the *hygroscopic* soot tested by Koehler et al. (2009). Their Aircraft Engine Combustor soot showed freezing only close to homogeneous freezing conditions for $T = 233$ K and 221.5 K, both for testing $d_\mathrm{m} = 250$ nm and polydisperse aerosol. Our ice nucleation results for FW200 reveal that the conditions for 1 % of the particles being activated in the cirrus regime are met at roughly the same RH across all temperatures, for a given aerosol size. The constant onset S_i indicates that the freezing

20 is in fact determined by pore size and soot-water contact angle, which determine water filling of the pores and subsequent homogeneous freezing, rather than the bulk aggregate size. The different onsets reported for the different particle sizes (see SI Fig. S1) suggest that the pore size distribution is a function of the overall soot aggregate size and the associated number density of spherules, forming these cavities (see Fig. 5). An exception are the results of $T = 233$ K, where the nucleation rate is likely too small for the volume of the pore water to freeze within the 16 s residence time of the particles in HINC (David et al., in

25 prep.b).

The isotherms of both lamp black soots, LB_OEC and LB_RC, resemble a type-III isotherm. Taking the (specific N_2) surface area into account, the isotherms are characterized by a small amount of sorbed water vapor at (nearly) saturated conditions of approximately an equivalent monolayer coverage (see Fig. 7b). Such a weak interaction of the water molecules with the soot is also reflected in our ice nucleation results, where we only observe a modest freezing ability on these soots, below S_i conditions

30 of homogeneous freezing of solution droplets. This suggest a more hydrophobic character, i.e. a high soot-water contact angle, and/or limited availability of pores of the correct size, which would inhibit pore-filling well below water saturation conditions (David et al., in prep.a). The lower affinity to water as compared to FW200 indicates a higher soot-water contact angle and is further supported by the relatively lower values of the C parameter (see Table B1). Furthermore, our TGA experiments indicate that these samples are mainly composed of pure carbon, so we can exclude absorption of water by OM for these

35 soots. This is further supported by the absence of a steep increase in AF at the homogeneous freezing line, indicating a lack

in the formation of solution droplets, which has been observed (e.g. by Koehler et al., 2009). However, care must be taken when comparing equivalent monolayer coverages, as they neglect the effect of water being taken up in patches into the porous structure of the soot aggregates. Our DVS runs reveal a slight hysteresis of the lamp black soots (see Fig. 7b) suggesting the presence of some mesopores, but again lie within the uncertainty of approximately $\Delta m = 0.75$ %. The availability of some

5   slit-like pores was also inferred from TEM images (SI Fig. S18). At the same time our TEM images reveal that both lamp black soots have significantly broader primary particle size distributions with overall larger mean spherules compared to e.g. FW200 as discussed above (see Sect. 3.3). Thus, for a given mobility diameter selected in the DMA, lamp black aggregates are composed of fewer spherules and thus likely contain less cavities formed by sintered spherules compared to soots with smaller spherules, lowering the probability that a sufficient number of pores of the right size (and contact angle) are present

10   (David et al., in prep.a). The presence of some mesopores is further supported by the shape of the water uptake curves of LB_OEC and LB_RC, which both show a non-linear increase for $RH_w \geq 90$ %, related to capillary condensation. Thus, we believe that the ice formation associated with LB_OEC and LB_RC is indeed caused by a PCF mechanism, but that the more hydrophobic character of these soots (higher water-soot contact angles) decreases the efficiency of this process compared with the more hydrophilic FW200. This interpretation is consistent with the slightly larger water uptake of the LB_RC compared

15   to the LB_OEC (see Fig. 7b), resulting in a slightly better ice nucleation ability of the LB_RC compared to the LB_OEC (see Fig. 3).

The water uptake of the FS sample is roughly six times larger than that of the lamp black samples at the highest RH, but does not show a strong increase at $RH > 80$ %(see Fig. 7a). We believe that this reduced water uptake of the FS is caused by a lack of mesopores and a prevalence of narrow micropores, which take up water as observed by the mass increase at

20   relatively low RH_w. Micropore water uptake has been reported for fullerenes (Hantal et al., 2010) and is further supported by the absence of any hysteresis of the desorption isotherm. Additionally, the presence of micropores on the FS is also supported by the rather large surface area compared to the lamp blacks (see Table B1) and is consistent with Ferry et al. (2002), who found liquid water to exist in micropores of soot particles produced by a kerosene burner down to temperatures of $T = 200$ K. Also the value of the C constant in the classical BET equation, describing the adsorbate-adsorbent interaction strength,

25   was found to be $C = 478$ (see Table B1). Such a high value of C is usually associated with narrow micropores (Thommes et al., 2015). Nonetheless, water within micropores is not able to nucleate ice via the PCF mechanism, as these pores are too small to allow formation of a critical ice embryo (e.g. Marcolli, 2014). The absence of any sharp increase along the water uptake isotherm of FS at high RH_w further suggests that the mass loss during TGA cannot be associated with hygroscopic material responsible for water sorption, as a similar (non linear) increase in water mass would be expected for OM (e.g. Zardini

30   et al., 2008). Altogether, the ice nucleation mechanism of FS remains inconclusive and requires further studies since the results from TGA and DVS do not give a consistent picture favoring either PCF or homogeneous freezing of solution droplets as the prevailing mechanism for the observed ice nucleation activity of this soot in the cirrus regime. Finally, the water sorption isotherms for the miniCAST samples reveal their general hydrophobic character, consistent with our ice nucleation results. In particular, it is worthwhile to note that the mCAST brown shows a reduced water uptake capacity compared to the mCAST

35   black. This supports our hypothesis from above, that the OM associated with mCAST brown is water-insoluble, suppressing

the ice nucleation activity possibly by filling the mesopores thus blocking water uptake in them. The larger water uptake of the mCAST black compared to the lamp blacks could result from a larger number of mesopores on the mCAST black aggregates, which are generally composed of more and smaller primary particles compared to the lamp blacks. This is consistent with the slightly larger hysteresis observed for the mCAST black sample compared to the lamp blacks. Mesopores are indeed present on most tested samples (with the exception of FS), as can be inferred from the DVS experiments and are consistent with ice nucleation below homogeneous freezing conditions of solution droplets for large enough soot aggregates (see Fig. 3). Combining our ice nucleation results with data obtained from TGA and DVS, we confidently identify PCF as the dominant mechanism to cause the freezing of the tested soots. Nevertheless, FW200 is the only sample out of the six probed soots that shows significant ice nucleation well below conditions for homogeneous freezing of solutions. Thus, the presence of pores (mechanical active sites) is insufficient for PCF, but the sites need to have a hydrophilic character in the form of hydrophilic surface functional groups to initiate interaction of the soot surface with water vapor within a pore, i.e. a sufficiently low contact angle (David et al., in prep.a).

4   Atmospheric implications

Our results are direct evidence that bare, large hydrophilic soot aggregates can nucleate ice via PCF. To what extent our results are transferable to atmospheric soot is discussed here. The absence of freezing below water saturation for $T > 233$ K suggests that the impact of soot on ice nucleation in MPCs is negligible, at least for unprocessed soot particles. For temperatures above 233 K our results show activation only above water saturation, indicating droplet formation for all of the soot types and sizes tested, confirming the results of Friedman et al. (2011), who found no heterogeneous ice formation at water subsaturated conditions at 233 K.

Our ice nucleation measurements of 400 nm size selected particles demonstrate that soot particles can nucleate ice in the cirrus regime, below RH for the homogeneous freezing of solution droplets, if the particles have the required physicochemical properties. Specifically, our DVS results reveal that both pore structure and contact angle determine the ice nucleation ability of the soots studied. In the case of extremely hydrophobic soot (very high soot-water contact angles), such as mCAST brown, the lack of ice nucleation below homogeneous freezing conditions of solution droplets, even for the largest particle sizes tested here, suggests that such soot does not play a role in atmospheric ice nucleation, at least for the cirrus temperatures covered by our experiments. However, slightly less hydrophobic soot (lamp blacks), still characterized by high soot-water contact angles, can promote ice nucleation heterogeneouosly for $d_\mathrm{m} \geq 200$ nm. This limits the relevance of the majority of freshly emitted soots for atmospheric ice nucleation at cirrus conditions, which are generally believed to be hydrophobic. In contrast, hydrophilic soot (FW200) has the capability to act as effective INP ($AF > 10^{-3}$ for $RH_\mathrm{w} \approx 80$ %, see SI Fig. S1h) even at sizes $d_\mathrm{m} > 100$ nm, making it potentially important for the anthropogenic forcing on global climate. Nevertheless, most of the combustion aerosols emitted into the atmosphere have significantly smaller diameters usually below 100 nm (e.g. Rose et al., 2006; Kim et al., 2001; Moore et al., 2017) and can represent more complex internal mixtures. Since none of the investigated soot types was ice nucleation active when particles of 100 nm mobility diameter were selected, it is unlikely that such small soot particles

act as INP unless they are mixed with soluble material. This finding is important for the fate of soot particles associated with aviation emissions in the atmosphere (Kärcher, 2018), which are generally found to be even smaller than 100 nm in diameter (Moore et al., 2017; Yu et al., 2017). Thus, the role of bare small soot particles would be limited to a condensation sink for semivolatile water-soluble species. However, there is increasing evidence for larger soot aggregates up to 1 μm in diameter in

5   the atmosphere (Posfai et al., 2003; Chakrabarty et al., 2014), mainly sourced from biomass burning and wildfires. In addition, atmospheric aerosol particles have been reported to contain large black carbon inclusions (up to 1 μm in diameter, Moffet et al., 2016). In regions of the atmosphere where these large soot particles are found, with the required physicochemical properties, these soot particles will be able to nucleate ice similar to the 400 nm particles discussed here. Finally, the results reported here only encompass soot particles that activate within the residence time of HINC ($\tau \approx 16$ s) and within a single cloud cycle.

10 However, ice nucleation in aircraft plumes happens rapidly as contrail formation becomes visible within approximately one wingspan behind the air plane due to the high local supersaturations. This corresponds to timescales of a few seconds after particle emission (Schumann and Heymsfield, 2017; Schumann, 2012) similar to the residence time in HINC and the high saturation ratios achieved towards the end of our RH scans. At the same time, the atmospheric life time of soot is around $5 - 7\,\text{days}$ (Jiao et al., 2014; Reddy and Boucher, 2007). During this time the soot aggregates undergo atmospheric processing,

15 for instance in the form of multiple cloud formation cycles. In case of ice nucleation via a PCF mechanism, pore ice can remain trapped within the cavities between the cloud cycles, thus particles could grow into macroscopic ice crystals, as soon as the $RH_\text{i} > 100$ %. Such a pre-activation effect has been discussed before (D' Albe, 1949; Fukuta, 1966; Mossop, 1956; Marcolli, 2016) and should be addressed in future work, as this may have implications for the enhanced freezing ability of soots in both the cirrus and MPC temperature regime. Moreover, the wettability (contact angle) of soot particles can increase (decrease),

20 as these particles undergo atmospheric processing. Even though the more hydrophobic soots tested here reveal only a weak ability to nucleate ice via PCF below homogeneous freezing conditions, this likely changes during atmospheric processing and subsequent cloud cycles, with significant implications for the role of soot in atmospheric ice nucleation.

5   Conclusions

The ice nucleation ability of a variety of soot types has been systematically evaluated in controlled laboratory measurements.

25 The soot types investigated cover a wide range of physicochemical properties as proxies of atmospheric soot particles, including different commercially available black carbons such as gas blacks (FW200), lamp blacks (LB_RC and LB_OEC) and fullerene soots (FS), as well as propane flame soot with different OM content derived from a miniCAST burner (mCAST black and mCAST brown). Ice nucleation was probed on dry, size selected aerosol particles, for four different sizes of 100, 200, 300 and 400 nm (mobility diameter), covering a temperature range between 253 and 218 K, using HINC. Ice nucleation activity

30 was investigated in relation to particle morphology deduced from TEM and coupled DMA-CPMA measurements, temperature dependent mass loss obtained from TGA analysis, as well as water vapor uptake capacity derived from DVS experiments.

The results discussed in this paper show that soot particles can contribute to ice formation below homogeneous freezing conditions of solution droplets only if particle diameters exceed $d_\text{m} > 100$ nm. One distinct finding of our work is that there is

a marked dependence on the HNT for all of the investigated soot types. In the MPC temperature regime no ice nucleation was observed below water saturation, while for some of the probed soots ice nucleation was observed below RH required for homogeneous freezing of solution droplets in the cirrus regime. This strongly suggests a dependence on liquid water for ice nucleation onto soot particles investigated here. We conclude that the ice formation process on the soots is best described by a PCF mechanism and an absence of deposition nucleation. Auxiliary measurements performed along with our ice nucleation experiments indicate that physical and chemical properties of combustion aerosol varied markedly and influenced the ice nucleation ability of the particles. The TEM results revealed the presence of cavities and pores on all soot types investigated. Nevertheless, the pore number density likely depends on primary soot spherule size. More importantly, the potential of pores to take up water through capillary condensation strongly depends on their size and the soot-water contact angle, i.e. the hydrophilicity of the soot, as revealed by our TGA and DVS measurements. The presence of hydrophobic matter on the soot aggregates impedes ice nucleation probably due to blocking of pores. Our TGA, however, is limited to an overall assessment of the presence of heat sensitive matter and conclusions about the chemical nature of this material is not possible and should be investigated in future studies. In addition, the water affinity obtained from the DVS measurements alone cannot be used to draw direct conclusions about the ice nucleation efficiency and/or freezing mechanism, but has to be related to surface area and spherule size. Our TEM evaluation indicates that spherule size influences the availability of pores. Future studies should focus on how atmospheric processes change the hydrophilicity (contact angle) of a given aggregate and spherule size in order to further our understanding of the interplay between pore size and number density and contact angle.

Appendix B: Auxiliary measurements for soot sample characterization

B1 BET surface area

Particle surface area was determined with the Autosorb-1MP surface area analyzer (Quantachrome, Odelzhausen, Germany) by N_2 adsorption using the BET method. Specific surface area values were determined from the linear BET plot of the N_2

5 isotherm up to $p/p° \approx 0.28$, where p is the equilirbium pressure and $p°$ denotes the saturation vapor pressure, assuming a N_2 molecular cross sectional area of $\sigma_{N2} = 16.2$ $\mathring{A}^2$, and a minimum of three adsorption points, using the linear form of the BET equation (Thommes et al., 2015):

$$\frac{p/p°}{n(1-p/p°)} = \frac{C-1}{n_m C}(p/p°) + \frac{1}{n_m C},$$ (B1)

where n is the total amount of nitrogen adsorbed on the particle system and n_m is the specific monolayer capacity. The constant

10 C, reported in Table B1 for the investigated soots, gives information about the shape of the isotherm (Gregg and Sing, 1982; Thommes et al., 2015). N_2 adsorption was conducted at the temperature of liquid N_2 (≈ 77 K). The primary factor determining the specific surface area is the primary particle size, with smaller primary particle sizes resulting in higher specific surface areas. Prior to determination of specific surface areas, soot samples were outgassed and dried in a desiccator. First, soot samples where outgassed at 323 K until pressure dropped below 300 mbar. Temperature was subsequently increased step-wise to 353 K and

15 the samples were dried for a period of 15 h at this temperature, under nearly vacuum conditions, before the surface area was determined.

Table B1. Detailed results of the specific surface area measurements for the soot samples as determined by N_2 adsorption following the BET-method. All specific surface area values, $a_{BET,N2}$, are given in units of $[m^2/g]$. The mean values are reported in Table 1. Besides, we report the values of the C parameter used in Eq. B1.

	$a_{BET,N2}$ (#1)	C (#1)	$a_{BET,N2}$ (#2)	C (#1)
FW200	524.3	896.3	528.2	650.9
LB_OEC	24.8	132.8	22.5	218.5
FS	271.6	455.8	258.3	500.0
LB_RC	23.2	135.3	22.8	181.4
mCAST black	121.0	118.3	118.8	115.1
mCAST brown	127.6	59.9	122.9	50.4

B2 Temperature dependent mass loss: Thermogravimetric analysis

The temperature dependent mass loss of the soot samples was determined using a thermogravimetric analysis. Soot powder was deposited into a platinum crucible and subsequently exposed to three different temperature stages in a Thermogravimetric

Analyzer. For the miniCAST samples, not available in powder form, soot was collected on 47 mm diameter quartz fiber filters (Tissuquartz Filters, Type 2500QAT-UP, Pall Inc.), using a 47 mm aluminum in-line filter holder. The filter holder was mounted at a distance of 10 cm downstream of the miniCAST exhaust pipe, using an air-cooled stainless-steel pipe. Soot aerosols were then carefully removed from the filter with a metal spatula prior to TGA analysis. During thermogravimetric analysis, mass

5 changes are continuously monitored while the heating program reported in Table B2 was applied to all samples. Time, sample weight, temperature and gas flows are continuously recorded during the heating program. For TGA analysis performed within this work, a sample purge flow of 30 mLmin^{-1} and a balance purge flow of 40 mLmin^{-1} was used. N_2 was used for both flows so that the sample only reacts to temperature due to thermal decomposition. For every experiment an equilibration time of approximately $1-2$ min was used before starting the TGA program. This is done in order to allow the (sample-) pan to

10 come to complete rest, as any swing movement of the pan can cause inaccurate mass measurements (Lapuerta et al., 2007). Lapuerta et al. (2007) reported a non-linear increase in loss of material with increasing heating rates, but found the difference to be below 10 % when heating rates were constrained to a maximum of 20 °Cmin^{-1}. Hence, our samples should not be affected, by using the maximum heating rate of 20 °Cmin-1 (see Table B2).

Table B2. Heating program used for thermogravimetric analysis of soots in a pure N_2 atmosphere.

Step	Specification
1	Isothermal at $T = 30$ °Cmin^{-1} for 5 min
2	Ramp 15 °Cmin^{-1} to $T = 350$ °C
3	Isothermal at $T = 350$ °C for 30 min
4	Ramp 15 °Cmin^{-1} to $T = 650$ °C
5	Isothermal at $T = 650$ °C for 15 min
6	Ramp 20 °Cmin^{-1} to $T = 1000$ °C
7	Isothermal at $T = 1000$ °C for 10 min
8	Ramp 30 °Cmin^{-1} to $T = 30$ °C

B3   Water uptake and loss: Dynamic Vapor Sorption

15 During DVS experiments, the sample is constantly weighed (against a reference) as the sample is exposed to changing RH in so-called RH_w-scans. Samples in powder form are placed in a metal pan to prevent static electrical loading and the total gas flow (H_2O and N_2) was held at a constant flow rate of 200 smLmin^{-1} throughout the experiment. RH_w is automatically scanned in predefined steps and the sample mass at quasi-equilibrium conditions is measured whenever the temporal change in sample weight falls below a defined threshold. Since a *constant* mass is not reached during DVS, we refer to these conditions as

20 *quasi*-equilibrium. The time needed to reach quasi-equilibrium conditions is dependent on the slow water adsorption kinetics (Popovitcheva et al., 2000) and is proportional to the surface area available for uptake. Here we considered a mass change rate

Table B3. Relative mass loss as determined by TGA analysis in a pure N_2 atmosphere. Mass loss (ML) for soot samples is expressed as cumulative, relative weight loss at a given reference temperature, and are given as percentage mass loss from initial weight. Reported values indicate mean values of two TGA experiments performed for a given soot type.

	ML_{100} °C	ML_{150} °C	ML_{200} °C	ML_{250} °C	ML_{300} °C	ML_{350} °C	ML_{650} °C	ML_{950} °C
LB_OEC	0.10	0.16	0.25	0.36	0.44	0.53	0.68	0.97
FS	1.85	2.27	2.60	2.92	3.24	3.97	22.95	33.37
FW200	6.88	7.64	8.04	8.52	9.35	10.67	22.66	31.43
LB_RC	0.090	0.16	0.24	0.41	0.57	0.75	0.93	2.80
mCAST black	0.94	1.18	1.34	1.44	1.48	1.48	5.27	15.62
mCAST brown	0.55	1.61	3.39	5.71	7.52	10.25	15.68	18.58

at/or below 0.0005 %min^{-1} to correspond to quasi-equilibrium conditions, for an approximate sample weight of 10 mg. Each soot sample was dried at 298 K for a period of 1000 min prior to the measurement of a sorption isotherm, in order to remove any sorbed water vapor, by flushing the soot samples with only N_2 at atmospheric pressure. DVS runs were performed at $T = 298$ K. Mass change was monitored in intervals of 5 % for 0 % $< RH_w < 30$ %, at 40 %, 60 % and 80 % in the medium

5 RH_w range and in steps of 3 % between 80 % and 98 % to investigate the presence of mesopores. Note that the FW200 was only probed in intervals of 20 % below $RH_w = 80$ %. Each soot type was probed for two independent experiments in the DVS and good agreement was found. Exceptions are the mCAST samples, which were only probed once in the DVS. The desorption was probed at the same RH_w values so that a hysteresis could be derived. Similar to the TGA, no out gassing at elevated temperature or high vacuum was performed, in order to preserve the original surface properties.

10 **B4 Soot aggregate morphology and effective density: DMA-CPMA measurements**

The Centrifugal Particle Mass Analyser uses two nested, rotating, charged metal cylinders between which injected particles can be selected based on mass. The two opposing electric and centrifugal forces, arising from the potential difference and the rotation, respectively, are used to classify particles by mass to electrical charge ratio (m/q). Details on its operation may be found in Olfert and Collings (2005). In conjunction with a DMA, density and mass mobility exponent (D_{fm}) of aerosol particles

15 can be determined. For this purpose, DMA-CPMA are coupled in series in such a way that aerosol particles are first sent into the DMA, classifying the particles by electrical mobility (selecting by drag:charge), resulting in a narrow size distribution. It should be noted that this distribution contains predominantly singly charged particles of the mobility diameter chosen, but is not perfectly monodisperse, with some fraction of larger, multiply charged particles also being present (see SI Fig. S15). The particles are subsequently passed through the CPMA, selecting monodisperse aerosol by mass to charge, and counted by a CPC

20 (Model 3776, TSI Inc.) downstream of the CPMA, operated at a flow rate of 0.3 Lmin^{-1}, yielding the number concentration of size and mass selected aerosol. For a given mobility size, the CPMA is operated in scanning mode, measuring the number

Table B4. Mass-mobility pre-factor, C, and fractal dimension, D_{fm}, derived from power-law fits of the form of Eq. (B4) to mass-mobility data shown in Fig. 4a. A D_{fm} value of 1 corresponds to a straight chain-like structure, whereas $D_{\text{fm}} = 3$ indicates a compact sphere like structure.

	C [kgm$^{-D_{\text{fm}}}$]	D_{fm} [-]
FW200	0.02	2.35
FS	0.17	2.50
LB_OEC	3.65	2.64
LB_RC	0.07	2.38
mCAST black	0.01	1.86
mCAST brown	0.01	2.31

concentration of particles at discrete mass set points. Due to the fractal like morphology of soot aggregates a range of different masses can correspond with a selected mobility diameter, such that soot particles with a more uniform morphology would have a narrower mass distribution (Dickau et al., 2016). The DMA-CPMA output function can be used to derive aerosol properties, such as the fractal dimension and the effective density. The effective density (ρ_{eff}, e.g. Dickau et al., 2016; Olfert et al., 2017;

5 Abegglen et al., 2015) is defined as the density particles would have if they were spherical, i.e. by the ratio of particle mass to particle spherical equivalent volume based on the selected mobility diameter in the DMA, d_{m}, given by (McMurry et al., 2002):

$$\rho_{eff} = \frac{6}{\pi}\frac{m_p}{d_{\text{m}}^3}. \tag{B2}$$

Here, m_p denotes the median mass obtained by fitting the mean mass spectral number density distribution from the CPMA

10 scan of the DMA-classified particles with a log normal distribution. Typically ρ_{eff} is expressed as a power law fit of the form:

$$\rho_{eff} = Cd_{\text{m}}^{(D_{\text{fm}}-3)}, \tag{B3}$$

where D_{fm} is the mass-mobility exponent and C is a constant pre-factor with units of kgm$^{-D_{\text{fm}}}$. The fractal dimension D_{fm} is a useful quantity to describe aerosol properties. D_{fm} can be inferred from the power-law relationships relating particle mobility and mass (Schmidt-Ott, 1988; Schmidt-Ott et al., 1990):

15 $$m_p = Cd_{\text{m}}^{D_{\text{fm}}}, \tag{B4}$$

where C is a constant called the mass-mobility pre-factor. Here, the fractal dimension of the soot particles was obtained by performing a least-square fit, using a power-law relationship of the form of Eq. (B4) applied to the mass-mobility data, where the median mass was used.

Appendix C: miniCAST

Within the miniCAST, the combustion process is interrupted by quenching the flame with N_2. While the quenching of the flame within the burner takes place at a fixed height, the flame size can be varied by changing the absolute flow of fuel gas and oxidation air, holding the C:O ratio, i.e. the flame chemistry constant. At the same time, changing the ratio of the fuel gas and

5   the oxidation air, or premixing the fuel gas with N_2 allows for a controlled adjustment of the C:O ratio. For a high absolute flow of fuel and oxidation air, the flame is large and thus is quenched relatively low within the flame. On the other hand, a small absolute flow of fuel and oxidation air causes the quenching to take place close to the flame tip. We aimed at comparing the ice nucleation abilities of combustion generated soot by varying organic carbon mass. We therefore altered both, the position of flame quenching and the ratio of fuel to oxidation air. The miniCAST was operated at two different test points (TP). We use the

10   fuel-air flame equivalence ratio, Φ, its inverse, the air-fuel ratio, λ, and the atomic carbon-to-oxygen ratio, C:O, to characterize the flame chemistry at the two TP.

The flame C:O ratio can be calculated based on the fuel and air densities at normal temperature and pressure (NTP) according to:

$$C:O = \frac{Q_f 10^{-3}}{Q_{ox} 10^{-3}} \cdot \frac{\rho_{f,NTP} F_{Cinfuel}}{\rho_{ox,NTP} F_{O2inair}}, \tag{C1}$$

15   where Q_f and Q_{ox} denote the fuel and oxidation air flow rates, respectively (see Table C1), $F_{Cinfuel}$ denotes the C-fraction in C_3H_8 (0.818), $F_{O2inair}$ the fraction of O_2 in air (0.232) and $\rho_{f,NTP}$ and $\rho_{ox,NTP}$ denote the mass densities of C_3H_8 (1.882 kgmol^{-1}) and air (1.205 kgmol^{-1}).

Assuming the combustion reaction to be:

$$C_3H_8 + 5O_2 \rightarrow 3CO_2 + 4H_2O, \tag{CR1}$$

20   we calculate Φ, as fuel-air mass ratio divided by the stoichiometric fuel-air ratio, given by:

$$\Phi = \frac{(m_f/m_{ox})}{(m_f/m_{ox})_{st}} = \frac{1}{\lambda}. \tag{C2}$$

Here m_f denotes the mass flow of C_3H_8, m_{ox} the mass flow of oxidation air and the subscript st, denotes the stoichiometric fuel-air ratio. Using reaction CR1 and a mass percentage of O_2 of 23.2 % the stoichiometric fuel-air ratio is given by:

$$(m_f/m_{ox})_{st} = \frac{44.096\,\mathrm{gmol}^{-1}}{5 \cdot 31.998\,\mathrm{gmol}^{-1}} \cdot \frac{23.2}{100} = 0.0639. \tag{C3}$$

25   Thus the combustion process is *fuel rich* for $\Phi > 1$ and $\lambda < 1$ and *fuel lean* combustion occurs for $\Phi < 1$ and $\lambda > 1$, where *lean* refers to conditions where fuel is the limiting reactant.

It should be noted that the parameters described above characterizing the flame chemistry, allow only for limited comparison with other studies, since they do not include additional factors such as the N_2 quench gas flow rate, Q_{N2}, the N_2 flow rate premixed to the fuel, $Q_{N2,mix}$, the dilution air flow Q_{dil} or any differences in burner geometries (Durdina et al., 2016), which

30   influence the soot characteristics. We use these parameters to characterize our miniCAST soot samples termed mCAST black and mCAST brown, as shown in Table C1.

Table C1. Summary of the settings for miniCAST Series 4200, used to produce mCAST black and mCAST brown presented in this study. Q_f denotes the volumetric C_3H_8 (fuel) flow[c], Q_{ox} the oxidation air[a] flow, $Q_{N2,mix}$ the N_2[b] flow premixed with the fuel, Q_{N2} the quench N_2[b] and Q_{dil} the dilution air[a] flow, respectively. All flows are given in units of standard $[\text{Lmin}^{-1}]$. λ, Φ and C:O indicate the air-fuel equivalence ratio, the fuel-air ratio and the atomic carbon:oxygen ratio, respectively, as described in the text.

Soot type	Q_f	Q_{ox}	$Q_{N2,mix}$	Q_{N2}	Q_{dil}	λ	Φ	C:O
mCAST black	0.06	1.55	0.0	7.5	20.0	1.0576	0.9455	0.2132
mCAST brown	0.06	1.42	0.25	7.5	20.0	0.9689	1.0321	0.2327

[a] VOC filtered (wall) synthetic air, [b] Carbagas 5.0 grade, [c] Carbagas quality 25

Appendix D: TEM sample preparation and evaluation

We used TEM to visualize the dimensions and morphology of the soot particles. Size selected soot particles were collected on standard Cu-TEM grids having 400 mesh with a single coated continuous carbon film (Quantifoil Micro Tools GmbH, Großlöbichau, Germany), using the Zurich Electron Microscope Impactor (ZEMI). ZEMI is a semi-automated, custom built

5   rotating drum impactor, holding a total of 24 TEM grids. The aerosol containing air stream is directed onto the TEM grid. Soot particles with inertia are impacted onto the TEM grid, while the surrounding gas molecules are laterally sucked away. A step motor (R208 Microstepping Driver, RMS Technologies, Carson City, USA), controlled over a LabView program allows to adjust the time period that each grid is exposed to the aerosol flow and the to control the sampling flow rate using a MFC (G-Series, MKS Instruments, Andover, USA). The distance between the exit of the nozzle and the impaction plate (TEM grid) can

10 mechanically be adjusted. Here, we used a constant flow rate of $1 \ \text{Lmin}^{-1}$ and varied the sampling time between $100 - 600$ s, depending on the number concentration of the size selected aerosol, in order to ensure a high enough loading of the TEM grid. Images of the aggregates were obtained from a JEOL TEM-1400+ (JEOL Ltd., Tokyo, Japan) with a LaB6 filament, operating at 120 kV. Finally, particle morphology and primary particle size were obtained upon image analysis using the MATLAB (R2017b, MathWorks Inc., Natick, USA) image analysis tool box. Therefore, a custom developed program in MATLAB was

15 used which reads in the intensity images obtained from TEM. The program then allows to select regions of interest (ROIs), where individual primary spherules were sized using MATLAB's *imellipse* function, using the average of the minor and major axis describing the ellipse. For each aggregate a minimum of 3 different ROIs were selected to ensure that more weight was not given to certain regions of the soot aggregates under investigation. A minmimum of around 100 primary particles were sized for each soot type.

Appendix E: Horizontal Ice Nucleation Chamber

E1 Uncertainty in temperature and relative humidity

The main uncertainty of the ice nucleation measurements results from uncertainties in temperature control and flow changes that alter the ratio of aerosol to sheath flow ratio, resulting in variations of the humidity profile across the aerosol lamina (located

5   at the chamber center). We report uncertainties in $S_\mathrm{w}/S_\mathrm{i}$ arising from the variability of humidities across the aerosol lamina and temperature uncertainty, thus capturing the possible range of humidity conditions experienced by any aerosol particles that are confined within the lamina. We first calculate the aerosol lamina coordinates and in a second step the supersaturation at these coordinates. Due to the horizontal orientation of the chamber walls and the absence of any internal buoyancy (convection), the velocity profile is simply given by (Rogers, 1988):

10   $$v(z) = \frac{3}{2}\bar{v}[1 - \frac{z^2}{(d/2)^2}], \tag{E1}$$

where z denotes the vertical height coordinate, $d/2 = 1$ cm the half width between the cold and warm walls and $\bar{v}$ the mean flow velocity given by the ratio of the total volumetric flow rate, $Q_{tot} = \int_{z=0}^{z=d} v(z)dz$, and the cross-sectional area of the chamber. Assuming that 50 % of the volumetric aerosol flow is on either side of the chamber center line (position of aerosol injector), the coordinates of the lamina limits, a and b, are found by integrating the flow profile symmetrically around the

15   center line until the integrated flow matches the given aerosol flow. Hence, a and b depend on the *ratio* of aerosol to sheath flow (F_{AP}/F_{sheath}).

The temperature at any location z within the chamber can be calculated from the linear temperature profile Rogers (1988):

$$T(z, \Delta T) = T_\mathrm{c} + \frac{\Delta T}{D}z, \tag{E2}$$

where T_c and T_w denote the temperature of the cold and warm plates, respectively, and $\Delta T = \frac{T_\mathrm{w}-T_\mathrm{c}}{d}$. Similarly, the linear

20   profile of vapor pressure with respect to ice, e_i is given by:

$$e_\mathrm{i}(z) = e_\mathrm{s,i}(T_\mathrm{c}) + \frac{e_\mathrm{s,i}(T_w) - e_\mathrm{s,i}(T_\mathrm{c})}{d}z, \tag{E3}$$

where $e_\mathrm{s,i}$ denotes the saturation vapor pressure with respect to ice after Murphy and Koop (2005).

Overall, the range of saturation ratio experienced by particles in the aerosol lamina is a function of the ratio of aerosol to sheath flow, F_{AP}/F_{sheath}, center temperature, T_{center}, and temperature difference between the two walls, ΔT, i.e.:

25   $$\Delta S_\mathrm{x,lam} = \Delta S_\mathrm{x,lam}(F_{AP}/F_{sheath}, T_{center}, \Delta T), \tag{E4}$$

where the subscript x denotes evaulation with respect to water (S_w) or with respect to ice (S_i). For a given F_{AP}/F_{sheath} and T_{center}, activation mostly took place for high RH_w, i.e. large ΔT values. Large values of ΔT (i.e. large values of RH) also result in larger uncertainties in RH, thus for a variety of F_{AP}/F_{sheath} and T_{center}, we report the calculated uncertainty and variation in $S_{x,lam}$ for a S_w,center value of 1.05 as an upper limit of RH uncertainty.
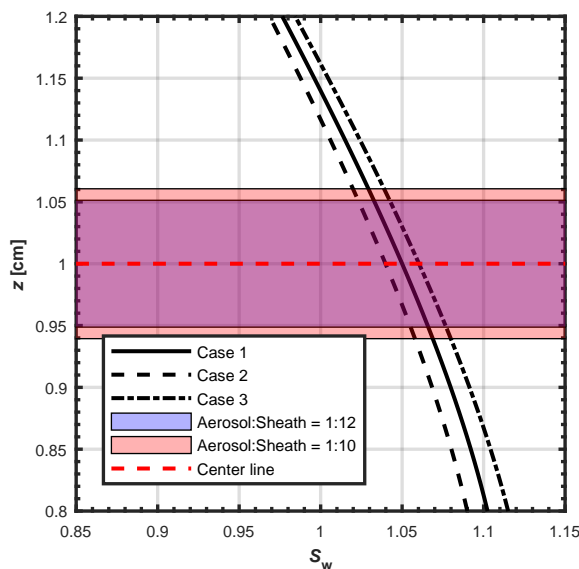
Figure E1. Example of S_w profile between cold ($z = 0$ cm, bottom) and warm ($z = 2$ cm, top) wall of the HINC chamber, illustrating the variations in S_w across the aerosol lamina (black solid line) for exemplary conditions of $T_{center} = 218$ K, $S_{w,center} = 1.05$ and different F_{AP}/F_{sheath} flow ratios (red and blue shading). The S_w profiles given by the dashed and dash-dotted lines take into into account uncertainty in temperature control arising from the thermocouples. The red dashed line indicates the position where particles are injected into HINC.

The temperatures can ultimately only be controlled within the uncertainty range of the thermocouples used for temperature control and monitoring, having an uncertainty of ± 0.1 K. Hence, for given conditions of F_{AP}/F_{sheath}, T_{center} and $S_{w,center}$, $\Delta S_{x,lam}(F_{AP}/F_{sheath}, T_{center}, \Delta T)$ was calculated for three different cases, covering the possible range of thermocouple uncertainties, but all leading to the same center conditions (T_{center}, $S_{w,center}$), namely:

5   – Case 1: $T_w = T_{w,set}$, $T_c = T_{c,set}$

   – Case 2: $T_w = T_{w,set} + 0.1$, $T_c = T_{c,set} - 0.1$

   – Case 3: $T_w = T_{w,set} - 0.1$, $T_c = T_{c,set} + 0.1$

The variation and uncertainty of the saturation profile across the aerosol lamina for these three cases is shown exemplarily in Fig. E1 for $T_{center} = 218$ K, $S_{w,center} = 1.05$ and different ratios of F_{AP}/F_{sheath}. In this study we use a flow ratio 10 $F_{AP}/F_{sheath} = 1 : 10$ to calculate our aerosol lamina boundaries and uncertainties associated with our ice nucleation results. Figure E2 finally illustrates the effect of flow ratio, i.e. aerosol lamina coordinates, on the overall uncertainty in RH across the aerosol lamina.
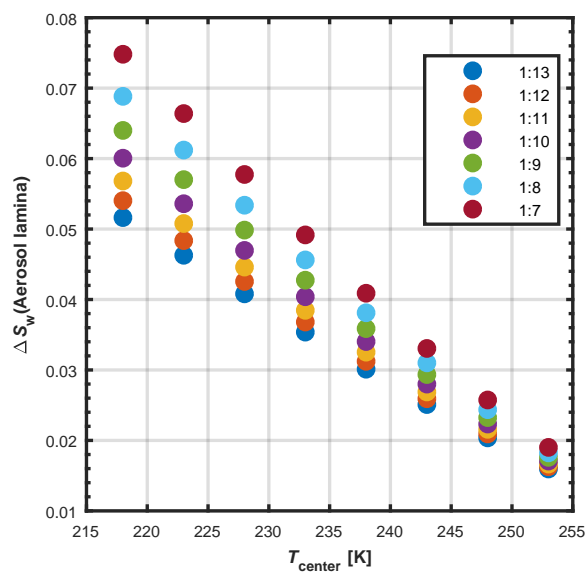
Figure E2. Relative humidity variation and uncertainty across the aerosol lamina, $\Delta S_{w,lam}$ as a function of T_{center} for different *ratios* of F_{AP}/F_{sheath} within HINC. Each reported value denotes the maximum spread in S_w across the aerosol lamina considering all three cases of TC-temperature uncertainty (see text) and a center S_w value of 1.05. The work presented here used flow ratios between 1:10 and 1:12.

Author contributions. FM prepared the manuscript with contributions from ZAK, CM, ROD, UL, EBM and PG. FM and ZAK designed the experiment. FM conducted and analyzed HINC measurements and prepared all figures of the manuscript. PG run DVS experiments and interpreted data. EBM took TEM images and helped with interpretation. FM, CM, ROD, UL and ZAK interpreted ice nucleation data. ZAK conceived the idea and supervised the overall project.

5   *Competing interests.* The authors declare that they have no conflict of interest.

Acknowledgements. F. Mahrt was funded by ETH Grant ETH-25-15-1. The authors gratefully acknowledge the great technical support of H. Wydler from the Institute for Atmosphere and Climate Science in overseeing the maintenance of HINC, improving both the CFDC and associated software as well as with help in developing ZEMI. We also thank M. Vecellio and P. Isler from the Institute for Atmosphere and Climate Science for machining parts of our set up. The authors would like to thank J.C.H. Wong from the Laboratory of Composite

10 Materials and Adaptive Structures for her training and help with the TGA and A. Röthlisberger, M. Rothaupt and M. Plötze from the Institute for Geotechnical Engineering for help with BET. The authors are grateful to I. Burgert from the Institute of Structural Engineering for providing access to the DVS facility. We also thank U. Krieger and S. Brunamonti from the Institute for Atmosphere and Climate Science for providing some of the soot samples and L. Lacher (KIT) and J. Atkinson for many helpful discussions on HINC and associated ice nucleation experiments. We thank J. Aerni for help with preparation of the TEM samples.

References

Abegglen, M., Durdina, L., Brem, B. T., Wang, J., Rindlisbacher, T., Corbin, J. C., Lohmann, U., and Sierau, B.: Effective density and mass-mobility exponents of particulate matter in aircraft turbine exhaust: Dependence on engine thrust and particle size, Journal of Aerosol Science, 88, 135–147, 2015.

Adachi, K., Chung, S. H., Friedrich, H., and Buseck, P. R.: Fractal parameters of individual soot particles determined using electron tomography: Implications for optical properties, Journal of Geophysical Research: Atmospheres, 112, n/a–n/a, 2007.

Archuleta, C. M., DeMott, P. J., and Kreidenweis, S. M.: Ice nucleation by surrogates for atmospheric mineral dust and mineral dust/sulfate particles at cirrus temperatures, Atmos. Chem. Phys., 5, 2617–2634, 2005.

Bescond, A., Yon, J., Ouf, F. X., Ferry, D., Delhaye, D., Gaffie, D., Coppalle, A., and Roze, C.: Automated Determination of Aggregate Primary Particle Size Distribution by TEM Image Analysis: Application to Soot, Aerosol Science and Technology, 48, 831–841, 2014.

Bond, T. C., Doherty, S. J., Fahey, D. W., Forster, P. M., Berntsen, T., DeAngelo, B. J., Flanner, M. G., Ghan, S., Kaercher, B., Koch, D., Kinne, S., Kondo, Y., Quinn, P. K., Sarofim, M. C., Schultz, M. G., Schulz, M., Venkataraman, C., Zhang, H., Zhang, S., Bellouin, N., Guttikunda, S. K., Hopke, P. K., Jacobson, M. Z., Kaiser, J. W., Klimont, Z., Lohmann, U., Schwarz, J. P., Shindell, D., Storelvmo, T., Warren, S. G., and Zender, C. S.: Bounding the role of black carbon in the climate system: A scientific assessment, Journal of Geophysical Research-Atmospheres, 118, 5380–5552, 2013.

Boucher, O.: Air traffic may increase cirrus cloudiness, Nature, 397, 30–31, 1999.

Bredin, A., Larcher, A. V., and Mullins, B. J.: Thermogravimetric analysis of carbon black and engine soot—Towards a more robust oil analysis method, Tribology International, 44, 1642–1650, 2011.

Brooks, S. D., Suter, K., and Olivarez, L.: Effects of chemical aging on the ice nucleation activity of soot and polycyclic aromatic hydrocarbon aerosols, J Phys Chem A, 118, 10 036–47, 2014.

Brunauer, S., Emmett, P. H., and Teller, E.: Adsorption of gases in multimolecular layers, Journal of the American Chemical Society, 60, 309–319, 1938.

Chakrabarty, R. K., Beres, N. D., Moosmüller, H., China, S., Mazzoleni, C., Dubey, M. K., Liu, L., and Mishchenko, M. I.: Soot superaggregates from flaming wildfires and their direct radiative forcing, Scientific Reports, 4, 5508, 2014.

Charnawskas, J. C., Alpert, P. A., Lambe, A. T., Berkemeier, T., O'Brien, R. E., Massoli, P., Onasch, T. B., Shiraiwa, M., Moffet, R. C., Gilles, M. K., Davidovits, P., Worsnop, D. R., and Knopf, D. A.: Condensed-phase biogenic-anthropogenic interactions with implications for cold cloud formation, Faraday Discussions, 200, 165–194, 2017.

Chou, C., Kanji, Z. A., Stetzer, O., Tritscher, T., Chirico, R., Heringa, M. F., Weingartner, E., Prevot, A. S. H., Baltensperger, U., and Lohmann, U.: Effect of photochemical ageing on the ice nucleation properties of diesel and wood burning particles, Atmospheric Chemistry and Physics, 13, 761–772, 2013.

Christenson, H. K.: Two-step crystal nucleation via capillary condensation, Crystengcomm, 15, 2030–2039, 2013.

Crawford, I., Moehler, O., Schnaiter, M., Saathoff, H., Liu, D., McMeeking, G., Linke, C., Flynn, M., Bower, K. N., Connolly, P. J., Gallagher, M. W., and Coe, H.: Studies of propane flame soot acting as heterogeneous ice nuclei in conjunction with single particle soot photometer measurements, Atmospheric Chemistry and Physics, 11, 9549–9561, 2011.

D' Albe, E. M. F.: Some experiments on the condensation of water vapour at temperatures below 0 °C, Quarterly Journal of the Royal Meteorological Society, 75, 1–14, 1949.

David, R. O., Fahrni, J., Marcolli, C., Mahrt, F., Brühwiler, D., Lohmann, U., and Kanji, Z. A.: The Role of Contact Angle and Pore Width on Pore Condensation and Freezing, in prep.a.

David, R. O., Marcolli, C., Fahrni, J., Qiu, Y., Perez Sirkin, Y. A., Molinero, V., Münch, S., Mahrt, F., Brühwiler, D., Lohmann, U., and Kanji, Z. A.: Is Deposition Ice Nucleation Real? The Role of Pore Condensation and Freezing on Atmospheric Ice Nucleation, in prep.b.

5 Demirdjian, B., Ferry, D., Suzanne, J., Popovicheva, O. B., Persiantseva, N. M., Kamaev, A. V., Shonija, N. K., and Zubareva, N. A.: Freezing of water adsorbed on hydrophobic and activated soot particles, Chemical Physics Letters, 480, 247–252, 2009.

DeMott, P. J.: An Exploratory Study of Ice Nucleation by Soot Aerosols, Journal of Applied Meteorology, 29, 1072–1079, 1990.

DeMott, P. J., Chen, Y., Kreidenweis, S. M., Rogers, D. C., and Sherman, D. E.: Ice formation by black carbon particles, Geophysical Research Letters, 26, 2429–2432, 1999.

10 DeMott, P. J., Petters, M. D., Prenni, A. J., Carrico, C. M., Kreidenweis, S. M., Collett, J. L., and Moosmüller, H.: Ice nucleation behavior of biomass combustion particles at cirrus temperatures, Journal of Geophysical Research: Atmospheres, 114, n/a–n/a, 2009.

Dickau, M., Olfert, J., Stettler, M. E. J., Boies, A., Momenimovahed, A., Thomson, K., Smallwood, G., and Johnson, M.: Methodology for quantifying the volatile mixing state of an aerosol, Aerosol Science and Technology, 50, 759–772, 2016.

Diehl, K. and Mitra, S. K.: A laboratory study of the effects of a kerosene-burner exhaust on ice nucleation and the evaporation rate of ice
15 crystals, Atmospheric Environment, 32, 3145–3151, 1998.

Dubinin, M. M.: Water-vapor adsorption and the microporous structures of carbonaceous adsorbents, Carbon, 18, 355–364, 1980.

Dubinin, M. M. and Stoeckli, H. F.: Homogeneous and heterogeneous micropore structures in carbonaceous adsorbents, Journal of Colloid and Interface Science, 75, 34–42, 1980.

Durdina, L., Lobo, P., Trueblood, M. B., Black, E. A., Achterberg, S., Hagen, D. E., Brem, B. T., and Wang, J.: Response of real-time black
20 carbon mass instruments to mini-CAST soot, Aerosol Science and Technology, 50, 906–918, 2016.

Dymarska, M., Murray, B. J., Sun, L., Eastwood, M. L., Knopf, D. A., and Bertram, A. K.: Deposition ice nucleation on soot at temperatures relevant for the lower troposphere, Journal of Geophysical Research: Atmospheres, 111, n/a–n/a, 2006.

Fan, J., Wang, Y., Rosenfeld, D., and Liu, X.: Review of Aerosol–Cloud Interactions: Mechanisms, Significance, and Challenges, Journal of the Atmospheric Sciences, 73, 4221–4252, 2016.

25 Ferry, D., Suzanne, J., Nitsche, S., Popovitcheva, O. B., and Shonija, N. K.: Water adsorption and dynamics on kerosene soot under atmospheric conditions, Journal of Geophysical Research-Atmospheres, 107, 2002.

Fornea, A. P., Brooks, S. D., Dooley, J. B., and Saha, A.: Heterogeneous freezing of ice on atmospheric aerosols containing ash, soot, and soil, Journal of Geophysical Research-Atmospheres, 114, 2009.

Friedman, B., Kulkarni, G., Beranek, J., Zelenyuk, A., Thornton, J. A., and Cziczo, D. J.: Ice nucleation and droplet formation by bare and
30 coated soot particles, Journal of Geophysical Research-Atmospheres, 116, 2011.

Fukuta, N.: Activation of Atmospheric Particles as Ice Nuclei in Cold and Dry Air, Journal of the Atmospheric Sciences, 23, 741–750, 1966.

Gorbunov, B., Baklanov, A., Kakutkina, N., Windsor, H. L., and Toumi, R.: Ice nucleation on soot particles, Journal of Aerosol Science, 32, 199–215, 2001.

Gregg, S. J. S. J. and Sing, K. S. W.: Adsorption, surface area and porosity, London ; New York : Academic Press, 2nd ed edn., 1982.

35 Hantal, G., Picaud, S., Hoang, P. N. M., Voloshin, V. P., Medvedev, N. N., and Jedlovszky, P.: Water adsorption isotherms on porous onionlike carbonaceous particles. Simulations with the grand canonical Monte Carlo method, The Journal of Chemical Physics, 133, 144 702, 2010.

Heymsfield, A., Baumgardner, D., DeMott, P., Forster, P., Gierens, K., and Kärcher, B.: Contrail Microphysics, Bulletin of the American Meteorological Society, 91, 465–472, 2010.

Higuchi, K. and Fukuta, N.: Ice in capillaries of solid particles and its effect on their nucleating ability, Journal of the Atmospheric Sciences, 23, 187–, 1966.

Hoose, C., Lohmann, U., Erdin, R., and Tegen, I.: The global influence of dust mineralogical composition on heterogeneous ice nucleation in mixed-phase clouds, Environmental Research Letters, 3, 2008.

5   Jiao, C., Flanner, M. G., Balkanski, Y., Bauer, S. E., Bellouin, N., Berntsen, T. K., Bian, H., Carslaw, K. S., Chin, M., De Luca, N., Diehl, T., Ghan, S. J., Iversen, T., Kirkevag, A., Koch, D., Liu, X., Mann, G. W., Penner, J. E., Pitari, G., Schulz, M., Seland, O., Skeie, R. B., Steenrod, S. D., Stier, P., Takemura, T., Tsigaridis, K., van Noije, T., Yun, Y., and Zhang, K.: An AeroCom assessment of black carbon in Arctic snow and sea ice, Atmospheric Chemistry and Physics, 14, 2399–2417, 2014.

Kanji, Z. A. and Abbatt, J. P. D.: Laboratory studies of ice formation via deposition mode nucleation onto mineral dust and n-hexane soot

10   samples, Journal of Geophysical Research-Atmospheres, 111, 2006.

Kanji, Z. A. and Abbatt, J. P. D.: The University of Toronto Continuous Flow Diffusion Chamber (UT-CFDC): A Simple Design for Ice Nucleation Studies, Aerosol Science and Technology, 43, 730–738, 2009.

Kanji, Z. A., DeMott, P. J., Moehler, O., and Abbatt, J. P. D.: Results from the University of Toronto continuous flow diffusion chamber at ICIS 2007: instrument intercomparison and ice onsets for different aerosol types, Atmospheric Chemistry and Physics, 11, 31–41, 2011.

15   Kanji, Z. A., Ladino, L. A., Wex, H., Boose, Y., Burkert-Kohn, M., Cziczo, D. J., and Krämer, M.: Overview of Ice Nucleating Particles, Meteorological Monographs, 58, 1.1–1.33, 2017.

Kim, W.-s., Kim, S. H., Lee, D. W., Lee, S., Lim, C. S., and Ryu, J. H.: Size Analysis of Automobile Soot Particles Using Field-Flow Fractionation, Environmental Science Technology, 35, 1005–1012, 2001.

Kireeva, E. D., Popovicheva, O. B., Persiantseva, N. M., Khokhlova, T. D., and Shonija, N. K.: Effect of black carbon particles on the

20   efficiency of water droplet freezing, Colloid Journal, 71, 353–359, 2009.

Kittaka, S., Ueda, Y., Fujisaki, F., Iiyama, T., and Yamaguchi, T.: Mechanism of freezing of water in contact with mesoporous silicas MCM-41, SBA-15 and SBA-16: role of boundary water of pore outlets in freezing, Physical Chemistry Chemical Physics, 13, 17 222–17 233, 2011.

Koehler, K. A., DeMott, P. J., Kreidenweis, S. M., Popovicheva, O. B., Petters, M. D., Carrico, C. M., Kireeva, E. D., Khokhlova, T. D., and

25   Shonija, N. K.: Cloud condensation nuclei and ice nucleation activity of hydrophobic and hydrophilic soot particles, Physical Chemistry Chemical Physics, 11, 7906–7920, 2009.

Koop, T., Luo, B. P., Tsias, A., and Peter, T.: Water activity as the determinant for homogeneous ice nucleation in aqueous solutions, Nature, 406, 611–614, 2000.

Kärcher, B.: Formation and radiative forcing of contrail cirrus, Nature Communications, 9, 1824, 2018.

30   Kärcher, B., Möhler, O., DeMott, P. J., Pechtl, S., and Yu, F.: Insights into the role of soot aerosols in cirrus cloud formation, Atmos. Chem. Phys., 7, 4203–4227, 2007.

Krätschmer, W., Lamb, L. D., Fostiropoulos, K., and Huffman, D. R.: Solid C60: a new form of carbon, Nature, 347, 354, 1990.

Kulkarni, G., China, S., Liu, S., Nandasiri, M., Sharma, N., Wilson, J., Aiken, A. C., Chand, D., Laskin, A., Mazzoleni, C., Pekour, M., Shilling, J., Shutthanandan, V., Zelenyuk, A., and Zaveri, R. A.: Ice nucleation activity of diesel soot particles at cirrus relevant temperature

35   conditions: Effects of hydration, secondary organics coating, soot morphology, and coagulation, Geophysical Research Letters, 43, 3580–3588, 2016.

Lacher, L., Lohmann, U., Boose, Y., Zipori, A., Herrmann, E., Bukowiecki, N., Steinbacher, M., and Kanji, Z. A.: The Horizontal Ice Nucleation Chamber (HINC): INP measurements at conditions relevant for mixed-phase clouds at the High Altitude Research Station Jungfraujoch, Atmospheric Chemistry and Physics, 17, 15 199–15 224, 2017.

Lapuerta, M., Ballesteros, R., and Rodríguez-Fernández, J.: Thermogravimetric analysis of diesel particulate matter, Measurement Science
5   and Technology, 18, 650, 2007.

Lohmann, U.: A glaciation indirect aerosol effect caused by soot aerosols, Geophysical Research Letters, 29, 11–1–11–4, 2002.

Lohmann, U.: AEROSOLS | Aerosol–Cloud Interactions and Their Radiative Forcing A2 - North, Gerald R, pp. 17–22, Academic Press, Oxford, https://doi.org/http://dx.doi.org/10.1016/B978-0-12-382225-3.00052-9, http://www.sciencedirect.com/science/article/pii/B9780123822253000529, 2015.

10 Lohmann, U. and Feichter, J.: Global indirect aerosol effects: a review, Atmospheric Chemistry and Physics, 5, 715–737, 2005.

Mamakos, A., Khalek, I., Giannelli, R., and Spears, M.: Characterization of Combustion Aerosol Produced by a Mini-CAST and Treated in a Catalytic Stripper, Aerosol Science and Technology, 47, 927–936, 2013.

Marcolli, C.: Deposition nucleation viewed as homogeneous or immersion freezing in pores and cavities, Atmos. Chem. Phys., 14, 2071–2104, 2014.

15 Marcolli, C.: Pre-activation of aeosol particles by pore condensation and freezing, Atmos. Chem. Phys. Discuss., 2016, 1–48, 2016.

McMurry, P. H., Wang, X., Park, K., and Ehara, K.: The Relationship between Mass and Mobility for Atmospheric Particles: A New Technique for Measuring Particle Density, Aerosol Science and Technology, 36, 227–238, 2002.

Möhler, O., Büttner, S., Linke, C., Schnaiter, M., Saathoff, H., Stetzer, O., Wagner, R., Krämer, M., Mangold, A., Ebert, V., and Schurath, U.: Effect of sulfuric acid coating on heterogeneous ice nucleation by soot aerosol particles, Journal of Geophysical Research: Atmospheres,
20 110, D11 210, 2005a.

Möhler, O., Linke, C., Saathoff, H., Schnaiter, M., Wagner, R., Mangold, A., Kramer, M., and Schurath, U.: Ice nucleation on flame soot aerosol of different organic carbon content, Meteorologische Zeitschrift, 14, 477–484, 2005b.

Moffet, R. C., O'Brien, R. E., Alpert, P. A., Kelly, S. T., Pham, D. Q., Gilles, M. K., Knopf, D. A., and Laskin, A.: Morphology and mixing of black carbon particles collected in central California during the CARES field study, Atmospheric Chemistry and Physics, 16,
25 14 515–14 525, 2016.

Moore, R. H., Ziemba, L. D., Dutcher, D., Beyersdorf, A. J., Chan, K., Crumeyrolle, S., Raymond, T. M., Thornhill, K. L., Winstead, E. L., and Anderson, B. E.: Mapping the Operation of the Miniature Combustion Aerosol Standard (Mini-CAST) Soot Generator, Aerosol Science and Technology, 48, 467–479, 2014.

Moore, R. H., Thornhill, K. L., Weinzierl, B., Sauer, D., D'Ascoli, E., Kim, J., Lichtenstern, M., Scheibe, M., Beaton, B., Beyersdorf, A. J.,
30 Barrick, J., Bulzan, D., Corr, C. A., Crosbie, E., Jurkat, T., Martin, R., Riddick, D., Shook, M., Slover, G., Voigt, C., White, R., Winstead, E., Yasky, R., Ziemba, L. D., Brown, A., Schlager, H., and Anderson, B. E.: Biofuel blending reduces particle emissions from aircraft engines at cruise conditions, Nature, 543, 411–+, 2017.

Mossop, S. C.: Sublimation Nuclei, Proceedings of the Physical Society. Section B, 69, 161, 1956.

Mueller, L., Jakobi, G., Orasche, J., Karg, E., Sklorz, M., Abbaszade, G., Weggler, B., Jing, L. P., Schnelle-Kreis, J., and Zimmermann, R.:
35 Online determination of polycyclic aromatic hydrocarbon formation from a flame soot generator, Analytical and Bioanalytical Chemistry, 407, 5911–5922, 2015.

Muller, J. O., Su, D. S., Jentoft, R. E., Krohnert, J., Jentoft, F. C., and Schlogl, R.: Morphology-controlled reactivity of carbonaceous materials towards oxidation, Catalysis Today, 102, 259–265, 2005.

Murphy, D. M. and Koop, T.: Review of the vapour pressures of ice and supercooled water for atmospheric applications, Quarterly Journal of the Royal Meteorological Society, 131, 1539–1565, 2005.

Olfert, J. S. and Collings, N.: New method for particle mass classification - the Couette centrifugal particle mass analyzer, Journal of Aerosol Science, 36, 1338–1352, 2005.

5 Olfert, J. S., Symonds, J. P. R., and Collings, N.: The effective density and fractal dimension of particles emitted from a light-duty diesel vehicle with a diesel oxidation catalyst, Journal of Aerosol Science, 38, 69–82, 2007.

Olfert, J. S., Dickau, M., Momenimovahed, A., Saffaripour, M., Thomson, K., Smallwood, G., Stettler, M. E. J., Boies, A., Sevcenco, Y., Crayford, A., and Johnson, M.: Effective density and volatility of particles sampled from a helicopter gas turbine engine, Aerosol Science and Technology, pp. 1–11, 2017.

10 Park, K., Kittelson, D. B., and McMurry, P. H.: Structural properties of diesel exhaust particles measured by transmission electron microscopy (TEM): Relationships to particle mass and mobility, Aerosol Science and Technology, 38, 881–889, 2004.

Petzold, A., Ogren, J. A., Fiebig, M., Laj, P., Li, S. M., Baltensperger, U., Holzer-Popp, T., Kinne, S., Pappalardo, G., Sugimoto, N., Wehrli, C., Wiedensohler, A., and Zhang, X. Y.: Recommendations for reporting "black carbon" measurements, Atmospheric Chemistry and Physics, 13, 8365–8379, 2013.

15 Popovicheva, O., Persiantseva, N. M., Shonija, N. K., DeMott, P., Koehler, K., Petters, M., Kreidenweis, S., Tishkova, V., Demirdjian, B., and Suzanne, J.: Water interaction with hydrophobic and hydrophilic soot particles, Physical Chemistry Chemical Physics, 10, 2332–2344, 2008.

Popovicheva, O. B., Persiantseva, N. M., Lukhovitskaya, E. E., Shonija, N. K., Zubareva, N. A., Demirdjian, B., Ferry, D., and Suzanne, J.: Aircraft engine soot as contrail nuclei, Geophysical Research Letters, 31, n/a–n/a, 2004.

20 Popovitcheva, O. B., Persiantseva, N. M., Trukhin, M. E., Rulev, G. B., Shonija, N. K., Buriko, Y. Y., Starik, A. M., Demirdjian, B., Ferry, D., and Suzanne, J.: Experimental characterization of aircraft combustor soot: Microstructure, surface area, porosity and water adsorption, Physical Chemistry Chemical Physics, 2, 4421–4426, 2000.

Portet-Koltalo, F. and Machour, N.: Analytical Methodologies for the Control of Particle-Phase Polycyclic Aromatic Compounds from Diesel Engine Exhaust, book section 4, InTech, Rijeka, https://doi.org/10.5772/53725, https://doi.org/10.5772/53725, 2013.

25 Posfai, M., Simonics, R., Li, J., Hobbs, P. V., and Buseck, P. R.: Individual aerosol particles from biomass burning in southern Africa: 1. Compositions and size distributions of carbonaceous particles, Journal of Geophysical Research-Atmospheres, 108, 2003.

Pruppacher, H. R. and Klett, D. J.: Microphysics of Clouds and Precipitation, Kluwer Academic Publishers, Dordrecht, The Netherlands, 2nd edition edn., 1997.

Ramanathan, V. and Carmichael, G.: Global and regional climate changes due to black carbon, Nature Geoscience, 1, 221–227, 2008.

30 Reddy, M. S. and Boucher, O.: Climate impact of black carbon emitted from energy consumption in the world's regions, Geophysical Research Letters, 34, 2007.

Rogers, D. C.: Development of a continuous flow thermal gradient diffusion chamber for ice nucleation studies, Atmospheric Research, 22, 149–181, 1988.

Rogers, D. C., DeMott, P. J., Kreidenweis, S. M., and Chen, Y.: Measurements of ice nucleating aerosols during SUCCESS, Geophysical
35 Research Letters, 25, 1383–1386, 1998.

Rogers, R. R. and Yau, M. K.: A short course in cloud physics, Pergamon Press, Oxford; New York, 1989.

Rose, D., Wehner, B., Ketzel, M., Engler, C., Voigtlander, J., Tuch, T., and Wiedensohler, A.: Atmospheric number size distributions of soot particles and estimation of emission factors, Atmospheric Chemistry and Physics, 6, 1021–1031, 2006.

Schill, G. P., Jathar, S. H., Kodros, J. K., Levin, E. J. T., Galang, A. M., Friedman, B., Link, M. F., Farmer, D. K., Pierce, J. R., Kreidenweis, S. M., and DeMott, P. J.: Ice nucleating particle emissions from photochemically-aged diesel and biodiesel exhaust, Geophysical Research Letters, pp. n/a–n/a, 2016.

Schmidt-Ott, A.: New approaches to in situ characterization of ultrafine agglomerates, Journal of Aerosol Science, 19, 553–563, 1988.

5 Schmidt-Ott, A., Baltensperger, U., Gaggeler, H. W., and Jost, D. T.: Scaling behavior of physical parameters describing agglomerates, Journal of Aerosol Science, 21, 711–717, 1990.

Schnaiter, M., Gimmler, M., Llamas, I., Linke, C., Jaeger, C., and Mutschke, H.: Strong spectral dependence of light absorption by organic carbon particles formed by propane combustion, Atmospheric Chemistry and Physics, 6, 2981–2990, 2006.

Schumann, U.: Formation, properties and climatic effects of contrails, Comptes Rendus Physique, 6, 549–565, 2005.

10 Schumann, U.: A contrail cirrus prediction model, Geoscientific Model Development, 5, 543–580, 2012.

Schumann, U. and Heymsfield, A. J.: On the Life Cycle of Individual Contrails and Contrail Cirrus, Meteorological Monographs, 58, 3.1–3.24, 2017.

Seinfeld, J. H.: Clouds, contrails and climate, Nature, 391, 837–838, 1998.

Sing, K. S. W., Everett, D. H., Haul, R. A. W., Moscou, L., Pierotti, R. A., Rouquerol, J., and Siemieniewska, T.: Reporting physisorption data
15 for gas solid systems with special reference to the determination of surface-area and porosity, Pure and Applied Chemistry, 57, 603–619, 1985.

Song, J. Z. and Peng, P. A.: Characterisation of black carbon materials by pyrolysis-gas chromatography-mass spectrometry, Journal of Analytical and Applied Pyrolysis, 87, 129–137, 2010.

Stratakis, G. A. and Stamatelos, A. M.: Thermogravimetric analysis of soot emitted by a modern diesel engine run on catalyst-doped fuel,
20 Combustion and Flame, 132, 157–169, 2003.

Suzanne, J., Ferry, D., Popovitcheva, O., and Shonija, N. K.: Ice nucleation by kerosene soot under upper tropospheric conditions, Canadian Journal of Physics, 81, 423–429, 2003.

Thommes, M., Kaneko, K., Neimark, A. V., Olivier, J. P., Rodriguez-Reinoso, F., Rouquerol, J., and Sing, K. S. W.: Physisorption of gases, with special reference to the evaluation of surface area and pore size distribution (IUPAC Technical Report), Pure and Applied Chemistry,
25 87, 1051–1069, 2015.

Vali, G., DeMott, P. J., Möhler, O., and Whale, T. F.: Technical Note: A proposal for ice nucleation terminology, Atmos. Chem. Phys., 15, 10 263–10 270, 2015.

Wang, H., Mao, Q. J., Cui, S. P., Zhang, L. J., and Lan, M. Z.: Study on the Volatility of Organic Contaminated Soil from Tar Workshop, Key Engineering Materials, 509, 93–98, 2012.

30 Welti, A., Luond, F., Stetzer, O., and Lohmann, U.: Influence of particle size on the ice nucleating ability of mineral dusts, Atmospheric Chemistry and Physics, 9, 6705–6715, 2009.

Welti, A., Kanji, Z. A., Lüönd, F., Stetzer, O., and Lohmann, U.: Exploring the Mechanisms of Ice Nucleation on Kaolinite: From Deposition Nucleation to Condensation Freezing, Journal of the Atmospheric Sciences, 71, 16–36, 2014.

Yon, J., Bescond, A., and Ouf, F. X.: A simple semi-empirical model for effective density measurements of fractal aggregates, Journal of
35 Aerosol Science, 87, 28–37, 2015.

Yu, Z. H., Liscinsky, D. S., Fortner, E. C., Yacovitch, T. I., Croteau, P., Herndon, S. C., and Miake-Lye, R. C.: Evaluation of PM emissions from two in-service gas turbine general aviation aircraft engines, Atmospheric Environment, 160, 9–18, 2017.

Zardini, A. A., Sjogren, S., Marcolli, C., Krieger, U. K., Gysel, M., Weingartner, E., Baltensperger, U., and Peter, T.: A combined particle

trap/HTDMA hygroscopicity study of mixed inorganic/organic aerosol particles, Atmos. Chem. Phys., 8, 5589–5601, 2008.